JUNE 23 2016

Near-field/far-field array manifold of an acoustic vector-sensor near a reflecting boundary

Yue Ivan Wu; Siu-Kit Lau; Kainam Thomas Wong

J. Acoust. Soc. Am. 139, 3159–3176 (2016)
https://doi.org/10.1121/1.4954253

Near-field/far-field array manifold of an acoustic vector-sensor near a reflecting boundary

Yue Ivan Wu
College of Computer Science, Sichuan University, 610065 Chengdu, Sichuan, China

Siu-Kit Lau
Department of Architecture, National University of Singapore, 4 Architecture Drive, 117566 Singapore

Kainam Thomas Wong[a)]
Department of Electronic and Information Engineering, Hong Kong Polytechnic University, Hung Hom, Kowloon, Hong Kong

(Received 29 July 2015; revised 20 May 2016; accepted 7 June 2016; published online 23 June 2016)

The acoustic vector-sensor (a.k.a. the vector hydrophone) is a practical and versatile sound-measurement device, with applications in-room, open-air, or underwater. It consists of three identical uni-axial velocity-sensors in orthogonal orientations, plus a pressure-sensor—all in spatial collocation. Its *far*-field array manifold [Nehorai and Paldi (1994). IEEE Trans. Signal Process. **42**, 2481–2491; Hawkes and Nehorai (2000). IEEE Trans. Signal Process. **48**, 2981–2993] has been introduced into the technical field of signal processing about 2 decades ago, and many direction-finding algorithms have since been developed for this acoustic vector-sensor. The above array manifold is subsequently generalized for outside the far field in Wu, Wong, and Lau [(2010). IEEE Trans. Signal Process. **58**, 3946–3951], but only if *no* reflection-boundary is to lie near the acoustic vector-sensor. As for the near-boundary array manifold for the general case of an emitter in the geometric near field, the far field, or anywhere in between—this paper derives and presents that array manifold in terms of signal-processing mathematics. Also derived here is the corresponding Cramér-Rao bound for azimuth-elevation-distance localization of an incident emitter, with the reflected wave shown to play a critical role on account of its constructive or destructive summation with the line-of-sight wave. The implications on source localization are explored, especially with respect to measurement model mismatch in maximum-likelihood direction finding and with regard to the spatial resolution between coexisting emitters. © *2016 Acoustical Society of America*. [http://dx.doi.org/10.1121/1.4954253]

[ZHM] Pages: 3159–3176

I. INTRODUCTION

Most acoustic sensors measure only the pressure of the acoustic wavefield, while over-looking the wavefield's underlying *particle velocity vector*, which represents a spatial gradient of the pressure field. This spatial gradient's three Cartesian components may be measured, each by a uni-axial velocity-sensor aligned along the corresponding Cartesian coordinate.[1] Hence, all three components of the particle velocity vector may be measured, at any spatial location, via three *uni*-axial velocity-sensors, placed in collocation but orthogonal orientations. Such a *tri*-axial velocity-sensor plus an isotropic pressure-sensor, together, is labeled an "acoustic **vector** sensor" (AVS) or a "vector hydrophone."[2] For comprehensive literature surveys on the AVS's hardware implementations or sea/air trials, please consult Tam and Wong (2009) and Wu and Wong (2012).

For an acoustic vector-sensor lying in an emitter's *far* field and *away* from any reflecting boundary (e.g., in deep sea scenarios), the measurement model has been developed in terms of signal processing mathematics by Nehorai and Paldi (1994). The corresponding signal processing mathematics for the not-necessarily-far-field (but still *no*-boundary) case has been advanced by Wu *et al.* (2010), showing a frequency-dependent gain and a frequency-dependent complex-phase, between the velocity-sensor triad on one hand and the pressure-sensor on the other hand.

In contrast to the above no-boundary models in Nehorai and Paldi (1994) and in Wu *et al.* (2010), boundaries are often present in acoustic propagation, e.g., underwater boundaries include the sea bottom, the sea surface, and ship hulls (Nagananda and Anand, 2010; Felisberto *et al.*, 2012), whereas air acoustic boundaries include walls and the ground (Levin *et al.*, 2010). For the *far*-field *near*-boundary case, the concerned measurement model has been advanced in Hawkes and Nehorai (2000), in terms of signal processing mathematics. Nonetheless, the not-necessarily-far-field[3] *near*-boundary measurement model is yet unavailable in a mathematical form easily comprehensible to signal-processing researchers unfamiliar with acoustical physics. For such a not-necessarily-far-field *near*-boundary case, this present paper will take Hawkes and Nehorai (2000) and Wu *et al.* (2010) one step further, to present its corresponding array manifold in terms of signal processing mathematics. This not-necessarily-far-field *near*-boundary array manifold depends on the reflection boundary's intrinsic physical properties. The special cases of a perfect-reflection boundary and a pressure-release reflection will receive special attention later in this paper.

a)Electronic mail: ktwong@ieee.org

II. TO DERIVE THE NEAR-BOUNDARY ARRAY-MANIFOLD—FOR THE NEAR FIELD, FAR FIELD, OR ANYWHERE IN BETWEEN

Consider the spatial geometry depicted in Fig. 1, which relates a point-size emitter, an acoustic vector-sensor, and a planar reflecting boundary. The acoustic vector-sensor is placed at the origin $\mathbf{r}_0 = [0,0,0]^T$ of the Cartesian coordinates without any loss of generality, where the superscript ^{T} denotes transposition. The point-size source emits isotropically from $\mathbf{r}_{\text{src}} = [x_{\text{src}}, y_{\text{src}}, z_{\text{src}}]^T$. The infinitely large reflecting plane lies at $z = -D$.[4] These result in an image source at $\mathbf{r}_{\text{mir}} = [x_{\text{src}}, y_{\text{src}}, -z_{\text{src}} - 2D]^T$. This spatial geometry has four independent parameters: D, ψ, R_{LOS}, and λ. Note that R_{re} and ψ' depend functionally on the four preceding parameters.

Suppose the point-size source emits a monochromatic signal, at an angular frequency of ω and amplitude of A, isotropically into a quiescent, isotropic, homogeneous fluid. The resulting wavefield may be represented as

$$p_{\text{in}}(\mathbf{r},t) = \frac{A}{\|\mathbf{r}-\mathbf{r}_{\text{src}}\|_2} \mathrm{e}^{\mathrm{j}[\omega t - \mathbf{k}_{\text{in}}^T(\mathbf{r}-\mathbf{r}_{\text{src}})]}, \tag{1}$$

at any time t and at any location $\mathbf{r} = [x,y,z]^T$. Here, the wave-number vector

$$\mathbf{k}_{\text{in}} = \frac{2\pi}{\lambda}\frac{\mathbf{r}-\mathbf{r}_{\text{src}}}{\|\mathbf{r}-\mathbf{r}_{\text{src}}\|_2}, \tag{2}$$

has a Frobenius norm of $\|\mathbf{k}_{\text{in}}\|_2 = k = 2\pi/\lambda$ and points along the wave's propagation direction.

Suppose this wave impinges upon a reflection boundary, at an incident angle ψ'. Then, $\mathbf{k}_{\text{in}}$ in Eq. (2) would be the incident wave-number vector, hence its subscript "in." The corresponding reflected wave would also be monochromatic

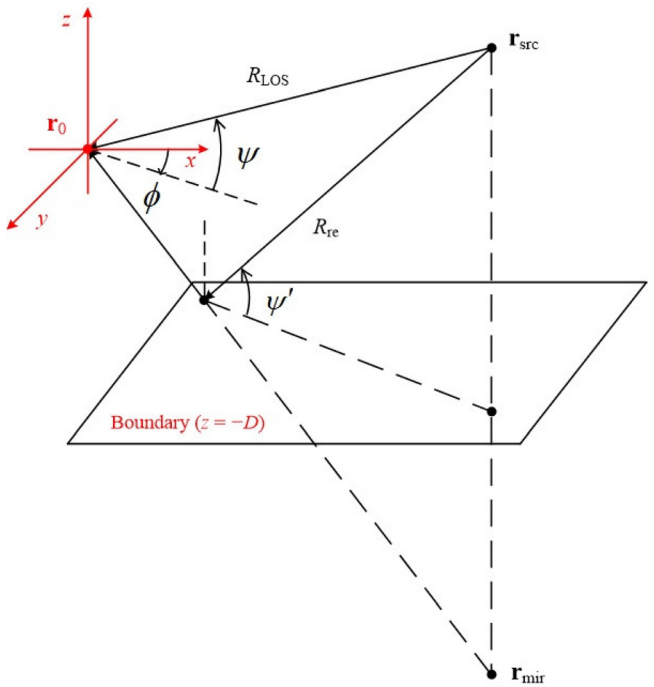

FIG. 1. (Color online) The spatial geometry among a point-size emitter, an acoustic vector-sensor, a planar reflecting boundary, and the image-source.

at the same angular frequency, but with a changed amplitude and a changed phase, such that the reflected wave may be represented as

$$p_{\text{re}}(\mathbf{r},t) = \frac{\Gamma(\mathbf{r},\omega)A}{\|\mathbf{r}-\mathbf{r}_{\text{mir}}\|_2} \mathrm{e}^{\mathrm{j}[\omega t - \mathbf{k}_{\text{re}}^T(\mathbf{r}-\mathbf{r}_{\text{mir}})]}, \tag{3}$$

wherein $\Gamma(\mathbf{r},\omega)$ symbolizes the "complex reflection coefficient," $\mathbf{k}_{\text{re}} = (2\pi/\lambda)(\mathbf{r}-\mathbf{r}_{\text{mir}}/\|\mathbf{r}-\mathbf{r}_{\text{mir}}\|_2)$ denotes the "reflected wave-number vector" at $\mathbf{r}$, with $\|\mathbf{k}_{\text{re}}\|_2 = k = (2\pi/\lambda)$ and $\mathbf{r}-\mathbf{r}_{\text{mir}} = [x-x_{\text{src}}, y-y_{\text{src}}, z+z_{\text{src}}+2D]^T$.

The superposition of the incident wave and the reflected wave gives

$$\begin{aligned} p_{\text{in}}(\mathbf{r},t) &= p_{\text{in}}(\mathbf{r},t) + p_{\text{re}}(\mathbf{r},t) \\ &= \underbrace{\left[\frac{\mathrm{e}^{-\mathrm{j}k\|\mathbf{r}-\mathbf{r}_{\text{src}}\|_2}}{\|\mathbf{r}-\mathbf{r}_{\text{src}}\|_2} + \frac{\Gamma(\mathbf{r},\omega)\mathrm{e}^{-\mathrm{j}k\|\mathbf{r}-\mathbf{r}_{\text{mir}}\|_2}}{\|\mathbf{r}-\mathbf{r}_{\text{mir}}\|_2}\right]}_{\stackrel{\text{def}}{=}\ a_p(\mathbf{r})} A\mathrm{e}^{\mathrm{j}\omega t}. \end{aligned} \tag{4}$$

At $\mathbf{r} = \mathbf{r}_0$ (where the acoustic vector-sensor is located)

$$p(\mathbf{r}_0,t) = \underbrace{\left[\frac{\mathrm{e}^{-\mathrm{j}kR_{\text{LOS}}}}{R_{\text{LOS}}} + \frac{\Gamma(\mathbf{r}_0,\omega)\mathrm{e}^{-\mathrm{j}kR_{\text{re}}}}{R_{\text{re}}}\right]}_{\stackrel{\text{def}}{=}\ a_p(\mathbf{r}_0)} A\mathrm{e}^{\mathrm{j}\omega t}, \tag{5}$$

with

$$R_{\text{LOS}} = \|\mathbf{r}_0 - \mathbf{r}_{\text{src}}\|_2 = \sqrt{x_{\text{src}}^2 + y_{\text{src}}^2 + z_{\text{src}}^2}, \tag{6}$$

$$R_{\text{re}} = \|\mathbf{r}_0 - \mathbf{r}_{\text{mir}}\|_2 = \sqrt{R_{\text{LOS}}^2 + 4Dz_{\text{src}} + 4D^2}, \tag{7}$$

respectively denoting the direct line-of-sight (LOS) distance from the emitter to the acoustic vector-sensor, and the distance between the image source and the acoustic vector-sensor.

The above acoustic *pressure* field $p(\mathbf{r},t)$ is related to its underlying *particle-velocity* field $\mathbf{v}(\mathbf{r},t)$ via Euler's equation, which is well known in fluid dynamics. That is,

$$\begin{aligned} \rho_0 \frac{\partial \mathbf{v}(\mathbf{r},t)}{\partial t} &= -\nabla p(\mathbf{r},t) \\ &= -\nabla[p_{\text{in}}(\mathbf{r},t) + p_{\text{re}}(\mathbf{r},t)], \end{aligned} \tag{8}$$

where ∇ represents the gradient operator $[\partial/\partial x, \partial/\partial y, \partial/\partial z]^T$ in the Cartesian coordinates. [Please see Eq. (6.2.7) on p. 243 in Morse and Ingard (1968), or Eq. (1.10) on p. 20 in Bies and Hansen (2009).] As the wave is sinusoidal

$$\begin{aligned} \rho_0 \frac{\partial \mathbf{v}(\mathbf{r},t)}{\partial t} &= \rho_0 \frac{\partial\left(|\mathbf{v}(\mathbf{r},t)|\mathrm{e}^{\mathrm{j}\omega t}\right)}{\partial t} \\ &= \rho_0 \mathrm{j}\omega \mathbf{v}(\mathbf{r},t). \end{aligned} \tag{9}$$

From Eqs. (4) to (9), the total acoustic particle-velocity field at $\mathbf{r}_0$ equals

$$\mathbf{v}(\mathbf{r}_0,t)=-\frac{1}{\mathrm{j}\omega\rho_0}[\nabla p(\mathbf{r},t)]|_{\mathbf{r}=\mathbf{r}_0}=\frac{A\mathrm{e}^{\mathrm{j}\omega t}}{-\mathrm{j}k\rho_0 c}\left[\frac{\partial a_p(\mathbf{r})}{\partial x}\Big|_{\mathbf{r}=\mathbf{r}_0},\ \frac{\partial a_p(\mathbf{r})}{\partial y}\Big|_{\mathbf{r}=\mathbf{r}_0},\ \frac{\partial a_p(\mathbf{r})}{\partial z}\Big|_{\mathbf{r}=\mathbf{r}_0}\right]^T. \tag{10}$$

Substituting $a_p(\mathbf{r})$ defined in Eq. (4) into Eq. (10), one obtains

$$\begin{aligned}
a_u(\mathbf{r}_0)&\overset{\text{def}}{=}\frac{\partial a_p(\mathbf{r})}{\partial x}\Big|_{\mathbf{r}=\mathbf{r}_0}\\
&=\frac{-\mathrm{j}k\mathrm{e}^{-\mathrm{j}k\|\mathbf{r}-\mathbf{r}_{\mathrm{src}}\|_2}\frac{\partial\|\mathbf{r}-\mathbf{r}_{\mathrm{src}}\|_2}{\partial x}\|\mathbf{r}-\mathbf{r}_{\mathrm{src}}\|_2-\mathrm{e}^{-\mathrm{j}k\|\mathbf{r}-\mathbf{r}_{\mathrm{src}}\|_2}\frac{\partial\|\mathbf{r}-\mathbf{r}_{\mathrm{src}}\|_2}{\partial x}}{\|\mathbf{r}-\mathbf{r}_{\mathrm{src}}\|_2^2}\Big|_{\mathbf{r}=\mathbf{r}_0}\\
&\quad+\frac{\left(\frac{\partial\Gamma(\mathbf{r},\omega)}{\partial x}\mathrm{e}^{-\mathrm{j}k\|\mathbf{r}-\mathbf{r}_{\mathrm{mir}}\|_2}-\mathrm{j}k\Gamma(\mathbf{r},\omega)\mathrm{e}^{-\mathrm{j}k\|\mathbf{r}-\mathbf{r}_{\mathrm{mir}}\|_2}\frac{\partial\|\mathbf{r}-\mathbf{r}_{\mathrm{mir}}\|_2}{\partial x}\right)\|\mathbf{r}-\mathbf{r}_{\mathrm{mir}}\|_2-\Gamma(\mathbf{r},\omega)\mathrm{e}^{-\mathrm{j}k\|\mathbf{r}-\mathbf{r}_{\mathrm{mir}}\|_2}\frac{\partial\|\mathbf{r}-\mathbf{r}_{\mathrm{mir}}\|_2}{\partial x}}{\|\mathbf{r}-\mathbf{r}_{\mathrm{mir}}\|_2^2}\Big|_{\mathbf{r}=\mathbf{r}_0}\\
&=\frac{-\mathrm{j}k\mathrm{e}^{-\mathrm{j}kR_{\mathrm{LOS}}}\frac{-x_{\mathrm{src}}}{R_{\mathrm{LOS}}}R_{\mathrm{LOS}}-\mathrm{e}^{-\mathrm{j}kR_{\mathrm{LOS}}}\frac{-x_{\mathrm{src}}}{R_{\mathrm{LOS}}}}{R_{\mathrm{LOS}}^2}+\frac{\left(\frac{\partial\Gamma(\mathbf{r},\omega)}{\partial x}\Big|_{\mathbf{r}=\mathbf{r}_0}\mathrm{e}^{-\mathrm{j}kR_{\mathrm{re}}}-\mathrm{j}k\Gamma(\mathbf{r}_0,\omega)\mathrm{e}^{-\mathrm{j}kR_{\mathrm{re}}}\frac{-x_{\mathrm{src}}}{R_{\mathrm{re}}}\right)R_{\mathrm{re}}-\Gamma(\mathbf{r},\omega)e^{-\mathrm{j}kR_{\mathrm{re}}}\frac{-x_{\mathrm{src}}}{R_{\mathrm{re}}}}{R_{\mathrm{re}}^2}\\
&=\frac{\mathrm{j}kR_{\mathrm{LOS}}+1}{R_{\mathrm{LOS}}^3}e^{-\mathrm{j}kR_{\mathrm{LOS}}}x_{\mathrm{src}}+\frac{\mathrm{e}^{-\mathrm{j}kR_{\mathrm{re}}}}{R_{\mathrm{re}}}\left[\frac{\mathrm{j}kR_{\mathrm{re}}+1}{R_{\mathrm{re}}^2}x_{\mathrm{src}}\Gamma(\mathbf{r}_0,\omega)+\frac{\partial\Gamma(\mathbf{r},\omega)}{\partial x}\Big|_{\mathbf{r}=\mathbf{r}_0}\right],
\end{aligned}$$

$$\begin{aligned}
a_v(\mathbf{r}_0)&\overset{\text{def}}{=}\frac{\partial a_p(\mathbf{r})}{\partial y}\Big|_{\mathbf{r}=\mathbf{r}_0}\\
&=\frac{-\mathrm{j}k\mathrm{e}^{-\mathrm{j}k\|\mathbf{r}-\mathbf{r}_{\mathrm{src}}\|_2}\frac{\partial\|\mathbf{r}-\mathbf{r}_{\mathrm{src}}\|_2}{\partial y}\|\mathbf{r}-\mathbf{r}_{\mathrm{src}}\|_2-\mathrm{e}^{-\mathrm{j}k\|\mathbf{r}-\mathbf{r}_{\mathrm{src}}\|_2}\frac{\partial\|\mathbf{r}-\mathbf{r}_{\mathrm{src}}\|_2}{\partial y}}{\|\mathbf{r}-\mathbf{r}_{\mathrm{src}}\|_2^2}\Big|_{\mathbf{r}=\mathbf{r}_0}\\
&\quad+\frac{\left(\frac{\partial\Gamma(\mathbf{r},\omega)}{\partial y}\mathrm{e}^{-\mathrm{j}k\|\mathbf{r}-\mathbf{r}_{\mathrm{mir}}\|_2}-\mathrm{j}k\Gamma(\mathbf{r},\omega)\mathrm{e}^{-\mathrm{j}k\|\mathbf{r}-\mathbf{r}_{\mathrm{mir}}\|_2}\frac{\partial\|\mathbf{r}-\mathbf{r}_{\mathrm{mir}}\|_2}{\partial y}\right)\|\mathbf{r}-\mathbf{r}_{\mathrm{mir}}\|_2-\Gamma(\mathbf{r},\omega)\mathrm{e}^{-\mathrm{j}k\|\mathbf{r}-\mathbf{r}_{\mathrm{mir}}\|_2}\frac{\partial\|\mathbf{r}-\mathbf{r}_{\mathrm{mir}}\|_2}{\partial y}}{\|\mathbf{r}-\mathbf{r}_{\mathrm{mir}}\|_2^2}\Big|_{\mathbf{r}=\mathbf{r}_0}\\
&=\frac{-\mathrm{j}k\mathrm{e}^{-\mathrm{j}kR_{\mathrm{LOS}}}\frac{-y_{\mathrm{src}}}{R_{\mathrm{LOS}}}R_{\mathrm{LOS}}-\mathrm{e}^{-\mathrm{j}kR_{\mathrm{LOS}}}\frac{-y_{\mathrm{src}}}{R_{\mathrm{LOS}}}}{R_{\mathrm{LOS}}^2}+\frac{\left(\frac{\partial\Gamma(\mathbf{r},\omega)}{\partial y}\Big|_{\mathbf{r}=\mathbf{r}_0}\mathrm{e}^{-\mathrm{j}kR_{\mathrm{re}}}-\mathrm{j}k\Gamma(\mathbf{r}_0,\omega)\mathrm{e}^{-\mathrm{j}kR_{\mathrm{re}}}\frac{-y_{\mathrm{src}}}{R_{\mathrm{re}}}\right)R_{\mathrm{re}}-\Gamma(\mathbf{r},\omega)e^{-\mathrm{j}kR_{\mathrm{re}}}\frac{-y_{\mathrm{src}}}{R_{\mathrm{re}}}}{R_{\mathrm{re}}^2}\\
&=\frac{\mathrm{j}kR_{\mathrm{LOS}}+1}{R_{\mathrm{LOS}}^3}e^{-\mathrm{j}kR_{\mathrm{LOS}}}y_{\mathrm{src}}+\frac{\mathrm{e}^{-\mathrm{j}kR_{\mathrm{re}}}}{R_{\mathrm{re}}}\left[\frac{\mathrm{j}kR_{\mathrm{re}}+1}{R_{\mathrm{re}}^2}y_{\mathrm{src}}\Gamma(\mathbf{r}_0,\omega)+\frac{\partial\Gamma(\mathbf{r},\omega)}{\partial y}\Big|_{\mathbf{r}=\mathbf{r}_0}\right],
\end{aligned}$$

$$\begin{aligned}
a_w(\mathbf{r}_0)&\overset{\text{def}}{=}\frac{\partial a_p(\mathbf{r})}{\partial z}\Big|_{\mathbf{r}=\mathbf{r}_0}\\
&=\frac{-\mathrm{j}k\mathrm{e}^{-\mathrm{j}k\|\mathbf{r}-\mathbf{r}_{\mathrm{src}}\|_2}\frac{\partial\|\mathbf{r}-\mathbf{r}_{\mathrm{src}}\|_2}{\partial z}\|\mathbf{r}-\mathbf{r}_{\mathrm{src}}\|_2-\mathrm{e}^{-\mathrm{j}k\|\mathbf{r}-\mathbf{r}_{\mathrm{src}}\|_2}\frac{\partial\|\mathbf{r}-\mathbf{r}_{\mathrm{src}}\|_2}{\partial z}}{\|\mathbf{r}-\mathbf{r}_{\mathrm{src}}\|_2^2}\Big|_{\mathbf{r}=\mathbf{r}_0}\\
&\quad+\frac{\left(\frac{\partial\Gamma(\mathbf{r},\omega)}{\partial z}\mathrm{e}^{-\mathrm{j}k\|\mathbf{r}-\mathbf{r}_{\mathrm{mir}}\|_2}-\mathrm{j}k\Gamma(\mathbf{r},\omega)\mathrm{e}^{-\mathrm{j}k\|\mathbf{r}-\mathbf{r}_{\mathrm{mir}}\|_2}\frac{\partial\|\mathbf{r}-\mathbf{r}_{\mathrm{mir}}\|_2}{\partial z}\right)\|\mathbf{r}-\mathbf{r}_{\mathrm{mir}}\|_2-\Gamma(\mathbf{r},\omega)\mathrm{e}^{-\mathrm{j}k\|\mathbf{r}-\mathbf{r}_{\mathrm{mir}}\|_2}\frac{\partial\|\mathbf{r}-\mathbf{r}_{\mathrm{mir}}\|_2}{\partial z}}{\|\mathbf{r}-\mathbf{r}_{\mathrm{mir}}\|_2^2}\Big|_{\mathbf{r}=\mathbf{r}_0}\\
&=\frac{-\mathrm{j}k\mathrm{e}^{-\mathrm{j}kR_{\mathrm{LOS}}}\frac{-z_{\mathrm{src}}}{R_{\mathrm{LOS}}}R_{\mathrm{LOS}}-\mathrm{e}^{-\mathrm{j}kR_{\mathrm{LOS}}}\frac{-z_{\mathrm{src}}}{R_{\mathrm{LOS}}}}{R_{\mathrm{LOS}}^2}\\
&\quad+\frac{\left(\frac{\partial\Gamma(\mathbf{r},\omega)}{\partial z}\Big|_{\mathbf{r}=\mathbf{r}_0}\mathrm{e}^{-\mathrm{j}kR_{\mathrm{re}}}-\mathrm{j}k\Gamma(\mathbf{r}_0,\omega)\mathrm{e}^{-\mathrm{j}kR_{\mathrm{re}}}\frac{z_{\mathrm{src}}+2D}{R_{\mathrm{re}}}\right)R_{\mathrm{re}}-\Gamma(\mathbf{r},\omega)e^{-\mathrm{j}kR_{\mathrm{re}}}\frac{z_{\mathrm{src}}+2D}{R_{\mathrm{re}}}}{R_{\mathrm{re}}^2}\\
&=\frac{\mathrm{j}kR_{\mathrm{LOS}}+1}{R_{\mathrm{LOS}}^3}e^{-\mathrm{j}kR_{\mathrm{LOS}}}z_{\mathrm{src}}+\frac{\mathrm{e}^{-\mathrm{j}kR_{\mathrm{re}}}}{R_{\mathrm{re}}}-\left[\frac{\mathrm{j}kR_{\mathrm{re}}+1}{R_{\mathrm{re}}^2}(z_{\mathrm{src}}+2D)\Gamma(\mathbf{r}_0,\omega)+\frac{\partial\Gamma(\mathbf{r},\omega)}{\partial z}\Big|_{\mathbf{r}=\mathbf{r}_0}\right],
\end{aligned}$$

where

$$\frac{\partial}{\partial x}\|\mathbf{r}-\mathbf{r}_{\text{src}}\|_2=\frac{\partial}{\partial x}\sqrt{(x-x_{\text{src}})^2+(y-y_{\text{src}})^2+(z-z_{\text{src}})^2}=\frac{x-x_{\text{src}}}{\|\mathbf{r}-\mathbf{r}_{\text{src}}\|_2},$$
$$\frac{\partial}{\partial x}\|\mathbf{r}-\mathbf{r}_{\text{mir}}\|_2=\frac{\partial}{\partial x}\sqrt{(x-x_{\text{src}})^2+(y-y_{\text{src}})^2+(z+z_{\text{src}}+2D)^2}=\frac{x-x_{\text{src}}}{\|\mathbf{r}-\mathbf{r}_{\text{mir}}\|_2},$$
$$\frac{\partial}{\partial y}\|\mathbf{r}-\mathbf{r}_{\text{src}}\|_2=\frac{\partial}{\partial y}\sqrt{(x-x_{\text{src}})^2+(y-y_{\text{src}})^2+(z-z_{\text{src}})^2}=\frac{y-y_{\text{src}}}{\|\mathbf{r}-\mathbf{r}_{\text{src}}\|_2},$$
$$\frac{\partial}{\partial y}\|\mathbf{r}-\mathbf{r}_{\text{mir}}\|_2=\frac{\partial}{\partial y}\sqrt{(x-x_{\text{src}})^2+(y-y_{\text{src}})^2+(z+z_{\text{src}}+2D)^2}=\frac{y-y_{\text{src}}}{\|\mathbf{r}-\mathbf{r}_{\text{mir}}\|_2},$$
$$\frac{\partial}{\partial z}\|\mathbf{r}-\mathbf{r}_{\text{src}}\|_2=\frac{\partial}{\partial z}\sqrt{(x-x_{\text{src}})^2+(y-y_{\text{src}})^2+(z-z_{\text{src}})^2}=\frac{z-z_{\text{src}}}{\|\mathbf{r}-\mathbf{r}_{\text{src}}\|_2},$$
$$\frac{\partial}{\partial z}\|\mathbf{r}-\mathbf{r}_{\text{mir}}\|_2=\frac{\partial}{\partial z}\sqrt{(x-x_{\text{src}})^2+(y-y_{\text{src}})^2+(z+z_{\text{src}}+2D)^2}=\frac{z+z_{\text{src}}+2D}{\|\mathbf{r}-\mathbf{r}_{\text{mir}}\|_2}.$$

Lastly, factor out the common factor $A\exp(\mathrm{j}\omega t)$, in $p(\mathbf{r}_0,t)$ of Eq. (5) and in $\mathbf{v}(\mathbf{r}_0,t)$ of Eq. (10), in order to obtain the acoustic vector-sensor's not-necessarily-far-field near-boundary array manifold

$$\mathbf{a}^{(\text{b})}=\begin{bmatrix} a_u(\mathbf{r}_0)\\ a_v(\mathbf{r}_0)\\ a_w(\mathbf{r}_0)\\ -\mathrm{j}k\rho_0 c\ a_p(\mathbf{r}_0)\end{bmatrix}, \tag{11}$$

in the Cartesian coordinates. The superscript's acronym "b" signifies that the acoustic vector-sensor lies near a reflecting boundary, but anywhere in the far field, the near field, or in between.

To better reveal this array manifold's dependence on the emitter's azimuth-elevation angle-of-arrival (ϕ,ψ) and dependence on the separation R_{LOS} between the emitter and the acoustic vector-sensor:

(i) Write $x_{\text{src}}=R_{\text{LOS}}\cos\phi\cos\psi$, $y_{\text{src}}=R_{\text{LOS}}\sin\phi\cos\psi$, and $z_{\text{src}}=R_{\text{LOS}}\sin\psi$, where $\phi\in(-\pi,\pi]$ and $\psi\in[0,\pi/2]$, as shown in Fig. 1.

(ii) Then multiply Eq. (11) by $R_{\text{LOS}}^2\mathrm{e}^{\mathrm{j}kR_{\text{LOS}}}/\mathrm{j}kR_{\text{LOS}}+1$.

These steps express Eq. (11) as Eq. (12), where $\breve{R}_{\text{LOS}}=R_{\text{LOS}}/\lambda$, $\breve{D}=D/\lambda$, and $\breve{R}_{\text{re}}=R_{\text{re}}/\lambda$.

$$\mathbf{a}^{(b)}=\begin{bmatrix}\dfrac{\alpha\gamma}{\mathrm{j}k}\dfrac{\partial\Gamma(\mathbf{r},\,\omega)}{\partial x}\Big|_{\mathbf{r}=\mathbf{r}_0}+\big[1+\alpha\beta\Gamma(\mathbf{r}_0,\,\omega)\big]\cos(\phi)\cos(\psi)\\ \dfrac{\alpha\gamma}{\mathrm{j}k}\dfrac{\partial\Gamma(\mathbf{r},\,\omega)}{\partial y}\Big|_{\mathbf{r}=\mathbf{r}_0}+\big[1+\alpha\beta\Gamma(\mathbf{r}_0,\,\omega)\big]\sin(\phi)\cos(\psi)\\ \dfrac{\alpha\gamma}{\mathrm{j}k}\dfrac{\partial\Gamma(\mathbf{r},\,\omega)}{\partial z}\Big|_{\mathbf{r}=\mathbf{r}_0}+\big[1-\alpha\beta\Gamma(\mathbf{r}_0,\,\omega)\big]\sin(\psi)-\dfrac{2\breve{D}}{\breve{R}_{\text{LOS}}}\alpha\beta\Gamma(\mathbf{r}_0,\,\omega)\\ -\rho_0 c\ \gamma\big[1+\alpha\Gamma(\mathbf{r}_0,\,\omega)\big]\end{bmatrix}, \tag{12}$$

$$\alpha=\frac{\breve{R}_{\text{LOS}}}{\breve{R}_{\text{re}}}\mathrm{e}^{-\mathrm{j}\left(\breve{R}_{\text{re}}-\breve{R}_{\text{LOS}}\right)}, \tag{13}$$

$$\beta=\frac{\breve{R}_{\text{LOS}}^2}{\breve{R}_{\text{re}}^2}\frac{\mathrm{j}\breve{R}_{\text{re}}+1}{\mathrm{j}\breve{R}_{\text{LOS}}+1}, \tag{14}$$

$$\gamma=\frac{\mathrm{j}\breve{R}_{\text{LOS}}}{\mathrm{j}\breve{R}_{\text{LOS}}+1}, \tag{15}$$

$$\breve{D}=kD, \tag{16}$$

$$\breve{R}_{\text{LOS}}=kR_{\text{LOS}}, \tag{17}$$

$$\breve{R}_{\text{re}}=kR_{\text{re}}=\sqrt{\breve{R}_{\text{LOS}}^2+4\breve{R}_{\text{LOS}}\breve{D}\sin(\psi)+4\breve{D}^2}. \tag{18}$$

A. Special case: The acoustic vector-sensor lying in the emitter's near field and near a *perfect-reflection* boundary

"Perfect reflection" occurs when an incident wave hits upon an ideal "rigid" boundary (a.k.a. an acoustically hard surface), whose reflection coefficient $\Gamma(\mathbf{r},\omega)=1$, $\forall\mathbf{r}$, $\forall\omega$. A perfect-reflection boundary would neither absorb nor transmit any energy of any incident wavefield. In air acoustics, rigid boundaries are approximately realized in the sea surface's air-water plane interface when incident from above

(Leighton, 2012), and in-room acoustics at sufficiently low frequencies (Gumerov and Duraiswami, 2001; Remillieux, 2012). In underwater acoustics, rigid boundaries are approximately realized in the seabed (Buckingham and Tolstoy, 1990; Luo *et al.*, 2012), and in a vessel's hull at sufficiently high frequencies (Hawkes and Nehorai, 2000).

The asymptotic condition of $\Gamma(\mathbf{r},\omega)=1, \forall \mathbf{r}, \forall \omega$ implies the following: $\partial\Gamma(\mathbf{r},\omega)/\partial x|_{\mathbf{r}=\mathbf{r}_0}=0$, $\partial\Gamma(\mathbf{r},\omega)/\partial y|_{\mathbf{r}=\mathbf{r}_0}=0$, $\partial\Gamma(\mathbf{r},\omega)/\partial z|_{\mathbf{r}=\mathbf{r}_0}=0$, and $\Gamma(\mathbf{r}_0,\omega)=1$. Consequently, Eq. (12) becomes[5]

$$\mathbf{a}^{(\text{rigid})}=\begin{bmatrix}\cos(\phi)\cos(\psi)[1+\alpha\beta]\\ \sin(\phi)\cos(\psi)[1+\alpha\beta]\\ \sin(\psi)\,[1-\alpha\beta]-2\alpha\beta\dfrac{\breve{D}}{\breve{R}_{\text{LOS}}}\\ -\rho_0 c\;\;\gamma(1+\alpha)\end{bmatrix}, \tag{19}$$

where α, β, γ, $\breve{D}$, and $\breve{R}_{\text{LOS}}$ have been defined earlier in Eqs. (13)–(17). The above superscript, rigid, refers to the acoustic vector-sensor lying close to a "rigid boundary" and lying in the emitter's not-necessarily-far field.

B. Special case: The acoustic vector-sensor lying in the emitter's not-necessarily-far field and near a *pressure-release* boundary

On a "pressure-release" boundary, $p_{\text{re}}(\mathbf{r}_b,t)=0$, which implies that the boundary's "normal specific impedance" $Z_{\text{in}}(\psi,\omega)$ equals zero. Thus, the reflection coefficient $\Gamma(\mathbf{r},\omega)=-1$, $\forall\mathbf{r}$, $\forall\omega$. The pressure-release boundary can approximate a vessel's hull at low frequencies (<1 kHz) (Ko, 1996; Hawkes and Nehorai, 2000). The pressure-release boundary also approximates the sea surface's air-water when incident from below (Buckingham and Tolstoy, 1990; Luo *et al.*, 2012; Leighton, 2012), hence relevant to a floating array or a towed array (Hawkes and Nehorai, 2000; p. 135 of Pierce, 1989).

The condition of $\Gamma(\mathbf{r},\omega)=-1$, $\forall\mathbf{r}$, $\forall\omega$ implies the following: $\partial\Gamma(\mathbf{r},\omega)/\partial x|_{\mathbf{r}=\mathbf{r}_0}=0$, $\partial\Gamma(\mathbf{r},\omega)/\partial y|_{\mathbf{r}=\mathbf{r}_0}=0$, $\partial\Gamma(\mathbf{r},\omega)/\partial z|_{\mathbf{r}=\mathbf{r}_0}=0$, $\Gamma(\mathbf{r}_0,\omega)=-1$. Therefore, Eq. (12) becomes

$$\mathbf{a}^{(\text{release})}=\begin{bmatrix}\cos(\phi)\cos(\psi)[1-\alpha\beta]\\ \sin(\phi)\cos(\psi)[1-\alpha\beta]\\ \sin(\psi)\,[1+\alpha\beta]+2\alpha\beta\dfrac{\breve{D}}{\breve{R}_{\text{LOS}}}\\ -\rho_0 c\;\;\gamma(1-\alpha)\end{bmatrix}, \tag{20}$$

where α, β, γ, $\breve{D}$, and $\breve{R}_{\text{LOS}}$ have been defined earlier in Eqs. (13)–(17). The above superscript, "release," refers to the acoustic vector-sensor lying near a pressure-release boundary and anywhere in the emitter's near or far field.

C. Special case: The acoustic vector-sensor lying in the emitter's *far*-field and near a boundary

Consider the asymptotically far-field case of $R_{\text{LOS}}\to\infty$. The not-necessarily-far-field acoustic vector-sensor now "degenerates" to a far-field acoustic vector-sensor, and the emitted spherical wavefront becomes planar at reception.

Therefore,

(i) $\dfrac{\partial\Gamma(\mathbf{r},\omega)}{\partial x}|_{\mathbf{r}=\mathbf{r}_0}\to 0$, $\dfrac{\partial\Gamma(\mathbf{r},\omega)}{\partial y}|_{\mathbf{r}=\mathbf{r}_0}\to 0$, $\dfrac{\partial\Gamma(\mathbf{r},\omega)}{\partial z}|_{\mathbf{r}=\mathbf{r}_0}\to 0$.

(ii) $\breve{R}_{\text{LOS}}/\breve{R}_{\text{re}}\to 1$ and $\breve{D}/\breve{R}_{\text{LOS}}\to 0$, which in turn imply $R_{\text{re}}-R_{\text{LOS}}\to 2\breve{D}\sin\psi$. These lead to $\alpha\to \text{e}^{-\text{j}2\breve{D}\sin\psi}$, $\beta\to 1$, and $\gamma\to 1$.

(iii) $\Gamma(\mathbf{r},\omega)\to\Gamma_p(\psi,\omega)=\sin\psi_{\text{re}}-Z_c/Z_{\text{in}}(\psi,\omega)/\sin\psi_{\text{re}}+Z_c/Z_{\text{in}}(\psi,\omega)$, where $\Gamma_p(\psi,\omega)$ denotes the boundary's plane-wave reflection coefficient and $Z_c=\rho_0 c$ refers to the medium's characteristic impedance. Please see Eq. (2) in Embleton *et al.* (1976), Eq. (2) in Stinson (1995), or Eq. (5) in Li and Lu (2004). The above $\Gamma_p(\psi,\omega)$ is independent of $\mathbf{r}$.

The above degenerates the earlier not-necessarily-far-field near-boundary array manifold Eq. (12) to a *far*-field near-boundary array manifold

$$\mathbf{a}^{(\text{far, b})}=\begin{bmatrix}\cos(\phi)\,\cos(\psi)\,[1+\Gamma_p(\psi,\,\omega)\text{e}^{-\text{j}2\breve{D}\sin\psi}]\\ \sin(\phi)\,\cos(\psi)\,[1+\Gamma_p(\psi,\,\omega)\text{e}^{-\text{j}2\breve{D}\sin\psi}]\\ \sin(\psi)\,[1-\Gamma_p(\psi,\,\omega)\text{e}^{-\text{j}2\breve{D}\sin\psi}]\\ -\rho_0 c\,[1+\Gamma_p(\psi,\,\omega)\text{e}^{-\text{j}2\breve{D}\sin\psi}]\end{bmatrix}. \tag{21}$$

The above superscript "far, b" signifies that the acoustic vector-sensor lies in the emitter's "far field" and lies near a reflecting "boundary." Equation (21) concurs with Eq. (8) in Hawkes and Nehorai (2000), which has "normalized away" $-\rho 0c$ from the last element.

D. Special case: The acoustic vector-sensor lying in the emitter's "not-necessarily-far field" and *not* near any boundary

In the absence of any reflection boundary, there would be no reflected wavefield to add to the direct LOS wavefield as in Eq. (4). Therefore, $\Gamma(\mathbf{r}_0,\omega)=0$ in Eqs. (5) and (12), and Eq. (12) would then degenerate to Eq. (16) of Wu *et al.* (2010), namely[6]

$$\mathbf{a}^{(\text{no-b})}=\begin{bmatrix}\cos(\phi)\cos(\psi)\\ \sin(\phi)\cos(\psi)\\ \sin(\psi)\\ \dfrac{-\rho_0 c}{\sqrt{1+\left(\dfrac{1}{\breve{R}_{\text{LOS}}}\right)^2}}\;\exp\left(j\arctan\dfrac{1}{\breve{R}_{\text{LOS}}}\right)\end{bmatrix}. \tag{22}$$

The above superscript "no-b" signifies that the acoustic vector-sensor may lie in the emitter's "not-necessarily-far field," and is not near any reflecting boundary.

Note that $\mathbf{a}^{(\text{rigid})}$ in Eq. (19), $\mathbf{a}^{(\text{release})}$ in Eq. (20), and $\mathbf{a}^{(\text{no-b})}$ in Eq. (22) together may be represented in a general form as

$$\mathbf{a}_{\kappa} = \begin{bmatrix} \cos(\phi)\cos(\psi)\,[1+\kappa\alpha\beta] \\ \sin(\phi)\cos(\psi)\,[1+\kappa\alpha\beta] \\ \sin(\psi)\,[1-\kappa\alpha\beta] - 2\kappa\alpha\beta\dfrac{\breve{D}}{\breve{R}_{\text{LOS}}} \\ -\rho_0 c\,\gamma[1+\kappa\alpha] \end{bmatrix}, \tag{23}$$

where $\kappa \in \{1,-1,0\}$ serves as an indicator, with $\kappa = 1$ for a perfect-reflection boundary, with $\kappa = -1$ for a pressure-release boundary, and with $\kappa = 0$ for no boundary. That is

$$\mathbf{a}_{\kappa} = \begin{cases} \mathbf{a}^{(\text{rigid})}, & \text{for} \quad \kappa = 1, \\ \mathbf{a}^{(\text{release}),} & \text{for} \quad \kappa = -1, \\ \mathbf{a}^{(\text{no-b})}, & \text{for} \quad \kappa = 0. \end{cases} \tag{24}$$

E. Special case: The acoustic vector-sensor lying in the emitter's *far*-field and *not* near any boundary

As $R_{\text{LOS}} \to \infty$ in Eq. (22), the not-necessarily-far-field near-boundary array manifold of Eq. (22) would further degenerate to a *far*-field *no*-boundary array manifold (Nehorai and Paldi, 1994) of

$$\mathbf{a}^{(\text{far, no-b})} = \begin{bmatrix} \cos(\phi) & \cos(\psi) \\ \sin(\phi) & \cos(\psi) \\ \sin(\psi) & \\ -\rho_0 c & \end{bmatrix}. \tag{25}$$

The above superscript "far, no-b" signifies that the source is in the far field and is not near any reflecting boundary. The fourth element in the above array-manifold (corresponding to the pressure amplitude) is sometimes normalized to unity, as in Eq. (2.5) of Nehorai and Paldi (1994).

III. VERIFICATION OF THE NEWLY DERIVED NEAR-BOUNDARY NEAR-FIELD ARRAY MANIFOLD, VIA FINITE ELEMENT METHOD (FEM)

For the perfect reflection boundary array manifold derived in Eq. (19) of Sec. II A, the array manifold is validated here by FEM using the "COMSOL Multiphysics—Acoustic Module" software. Here, the pressure field and particle-velocity field are calculated for a pure-tone signal at signal-frequencies in 50 to 100 Hz, under air acoustical conditions. The FEM simulation results are shown in Figs. 2 and 3, both demonstrating the closeness of the FEM simulation to the derived Eq. (19), thereby verifying the derivation in Sec. II A.

Figure 2's scenario is as follows: $R_{\text{LOS}} = 3.46\,\text{m}$, $D = 3.46\,\text{m}$, $\psi = 30°$, $\phi = -42°$, and $\rho_0 = 1.18\,\text{kg/m}^3$, $c = 346\,\text{m/s}$ in 25 °C air. This is not grazing incidence, which has been defined as $R_{\text{LOS}}\cos\psi \gg 2D + R_{\text{LOS}}\sin\psi$ [or equivalently $\sin(\pi/4 - \psi) \gg \sqrt{2}D/R_{\text{LOS}}$] below Eq. (19) of Attenborough (2002).

Figure 3 tries out a different scenario: $R_{\text{LOS}} = 1.73\,\text{m}$, $D = 3.46\,\text{m}$, $\psi = 45°$, $\phi = 23°$, with $\rho_0 = 1.18\,\text{kg/m}^3$ and $c = 346\,\text{m/s}$ in 25 °C air.

Figures 2 and 3 each plots the derived Eq. (19), which is a complex-valued vector function of frequency, as three curves. The solid curve plots the real-value part of $[\mathbf{a}^{(\text{rigid})}]_1/[\mathbf{a}^{(\text{rigid})}]_4$ versus its imaginary-value part, at various frequencies. Here, $[\cdot]_j$ denotes the jth entry of the vector

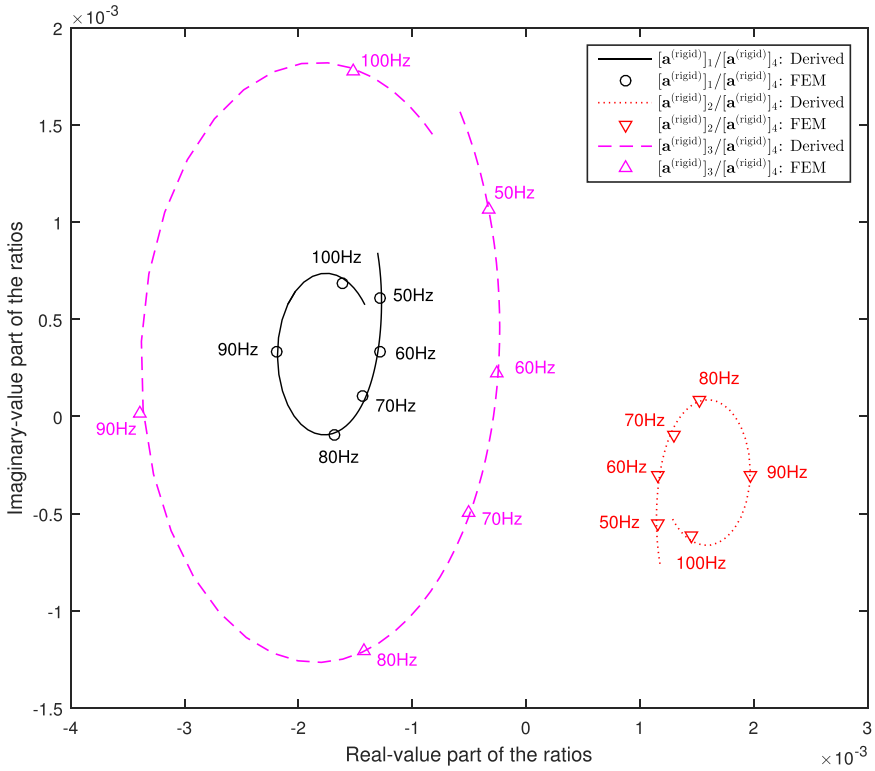

FIG. 2. (Color online) The ratio between (i) the particle velocity vector's each Cartesian component to (ii) the pressure. Here, $R_{\text{LOS}} = 3.46\,\text{m}$, $D = 3.46\,\text{m}$, $\psi = 30°$, $\phi = -42°$, with $\rho_0 = 1.18\,\text{kg/m}^3$ and $c = 346\,\text{m/s}$ for 25 °C air.

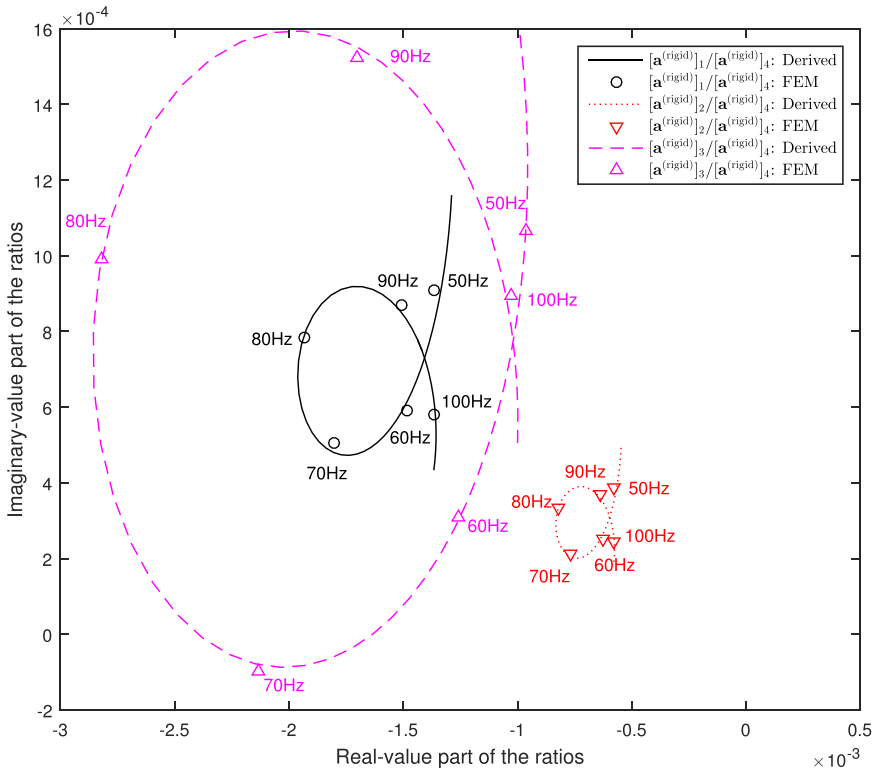

FIG. 3. (Color online) The ratio between (i) the particle velocity vector's each Cartesian component to (ii) the pressure. Here, $R_{\mathrm{LOS}} = 1.73\,\mathrm{m}$, $D = 3.46\,\mathrm{m}$, $\psi = 45°$, $\phi = 23°$, with $\rho_0 = 1.18\,\mathrm{kg/m^3}$ and $c = 346\,\mathrm{m/s}$ for 25 °C air.

inside the square brackets. The dotted curve does the same for $[\mathbf{a}^{(\mathrm{rigid})}]_2/[\mathbf{a}^{(\mathrm{rigid})}]_4$. Last, the dashed curve corresponds to $[\mathbf{a}^{(\mathrm{rigid})}]_3/[\mathbf{a}^{(\mathrm{rigid})}]_4$. The circle icons, the down-pointing triangle icons, and the up-pointing triangle icons, respectively, indicate the values calculated from FEM. The frequency value is indicated next to each icon. As this frequency varies from 50 to 100 Hz, R_{LOS} and D would correspondingly vary from 0.5 λ to λ. In both figures, the derived measurement model in Eq. (19) gives values very close to those calculated from FEM.

IV. CRAMÉR-RAO BOUND FOR 3D SOURCE LOCALIZATION USING AN ACOUSTIC VECTOR-SENSOR NEAR A *PERFECT-REFLECTION/PRESSURE-RELEASE* BOUNDARY, OR NO BOUNDARY

To further characterize the newly obtained array manifolds, this section will derive their Cramér-Rao bounds (CRB) for the localization of a source in three-dimensional (3D) space (i.e., azimuth/elevation/distance).[7]

To avoid distraction from the above objective, a very simple statistical model will be used below for the signal/noise statistics: The emitted signal $s(t) = \mathrm{e}^{\mathrm{j}(\omega t+\epsilon)}$ is a pure tone, at an angular frequency of ω, with an initial phase of ε, where both ω and ε are deterministic constants that are prior known to the estimator. At the mth time-instant at $t = mT_s$, a 4×1 data-vector

$$\tilde{\mathbf{z}}(mT_s) = \mathbf{a}_{\boldsymbol{\kappa}} s(mT_s) + \tilde{\mathbf{n}}(mT_s), \tag{26}$$

is collected by the four-component acoustic vector-sensor, where T_s refers to the time-sampling period, and $\tilde{\mathbf{n}}(t)$ denotes a 4×1 vector of additive zero-mean spatio-temporally uncorrelated Gaussian noise, each component of which has an unknown deterministic variance of σ^2.

With M number of time-samples, the collected data-set equals

$$\begin{aligned}\mathbf{z} &= [(\tilde{\mathbf{z}}(T_s))^T, \ldots, (\tilde{\mathbf{z}}(MT_s))^T]^T \\ &= \underbrace{\mathbf{s}\otimes\mathbf{a}_{\boldsymbol{\kappa}}}_{=\mu} + \underbrace{[(\tilde{\mathbf{n}}(T_s))^T, \ldots, (\tilde{\mathbf{n}}(MT_s))^T]^T}_{=\mathbf{n}},\end{aligned} \tag{27}$$

where $\mathbf{s} = \mathrm{e}^{\mathrm{j}\epsilon}[\mathrm{e}^{\mathrm{j}T_s\omega}, \mathrm{e}^{\mathrm{j}2T_s\omega}, \ldots, \mathrm{e}^{\mathrm{j}MT_s\omega}]^T$, $\otimes$ symbolizes the Kronecker product, $\mathbf{n}$ represents a $4M\times 1$ noise vector with a spatio-temporal covariance matrix of $\mathbf{C} = \sigma^2\mathbf{I}_{4M}$, and $\mathbf{I}_{4M}$ denotes a $4M\times 4M$ identity matrix. Therefore, $\mathbf{z}\sim\mathcal{N}(\mu,\mathbf{C})$.

Collecting the four unknown but deterministic parameters into a 4×1 vector $\theta = [\phi, \psi, \breve{R}_{\mathrm{LOS}}, \sigma^2]^T$, the resulting 4×4 Fisher Information Matrix (FIM) $\mathbf{J}(\theta)$ has an (i,j) th entry (Van-Trees, 2002) of

$$\begin{aligned}J_{i,j} = 2\,\mathrm{Re}&\left\{\left(\frac{\partial\mu}{\partial[\theta]_i}\right)^H\mathbf{C}^{-1}\left(\frac{\partial\mu}{\partial[\theta]_j}\right)\right\} \\ &+ \mathrm{Tr}\left\{\mathbf{C}^{-1}\frac{\partial\mathbf{C}}{\partial[\theta]_i}\mathbf{C}^{-1}\frac{\partial\mathbf{C}}{\partial[\theta]_j}\right\},\end{aligned} \tag{28}$$

where $\mathrm{Re}\{\cdot\}$ signifies the real-value part of the entity inside the curly brackets, $\mathrm{Tr}\{\cdot\}$ denotes the trace operation, and $[\cdot]_i$ symbolizes the ith element of the vector inside the square brackets.

Straight-forward manipulation of Eq. (28) gives $J_{1,2} = J_{1,3} = J_{1,4} = J_{2,1} = J_{2,4} = J_{3,1} = J_{3,4} = J_{4,1} = J_{4,2} = J_{4,3} = 0$, thereby leading to the simplification

$$\mathbf{J}(\theta)=\begin{bmatrix} J_{1,1} & 0 & 0 & 0 \\ 0 & J_{2,2} & J_{2,3} & 0 \\ 0 & J_{3,2} & J_{3,3} & 0 \\ 0 & 0 & 0 & J_{4,4} \end{bmatrix}. \tag{29}$$

The above implies that ϕ, $\{\psi, \breve{R}_{\mathrm{LOS}}\}$, and σ^2 are decoupled as three subgroups, and that the Cramér-Rao bounds of ϕ, ψ, $\breve{R}_{\mathrm{LOS}}$, respectively, equal

$$\begin{aligned}\mathrm{CRB}_{\phi} &= \lfloor \mathbf{J}^{-1}(\theta) \rfloor_{1,1} = \frac{1}{J_{1,1}} \\ &= \frac{\sigma^2}{2M}\frac{\left(1+\breve{R}_{\mathrm{LOS}}^2\right)\breve{R}_{\mathrm{re}}^6}{\cos^2\psi}\Big[\kappa^2\breve{R}_{\mathrm{LOS}}^6+\breve{R}_{\mathrm{re}}^6 \\ &\quad +\breve{R}_{\mathrm{LOS}}^2\breve{R}_{\mathrm{re}}^2\left(\kappa^2\breve{R}_{\mathrm{LOS}}^4+\breve{R}_{\mathrm{re}}^4\right) \\ &\quad +2\kappa\breve{R}_{\mathrm{LOS}}^3\breve{R}_{\mathrm{re}}^3\left(\breve{R}_{\mathrm{LOS}}\breve{R}_{\mathrm{re}}+1\right)\cos\left(\breve{R}_{\mathrm{LOS}}-\breve{R}_{\mathrm{re}}\right) \\ &\quad +2\kappa\left(\breve{R}_{\mathrm{LOS}}-\breve{R}_{\mathrm{re}}\right)\breve{R}_{\mathrm{LOS}}^3\breve{R}_{\mathrm{re}}^3\sin\left(\breve{R}_{\mathrm{LOS}}-\breve{R}_{\mathrm{re}}\right)\Big]^{-1},\end{aligned} \tag{30}$$

$$\mathrm{CRB}_{\psi} = \lfloor \mathbf{J}^{-1}(\theta) \rfloor_{2,2} = \frac{J_{3,3}}{J_{2,2}J_{3,3}-J_{2,3}J_{3,2}}, \tag{31}$$

$$\mathrm{CRB}_{\breve{R}_{\mathrm{LOS}}} = \lfloor \mathbf{J}^{-1}(\theta) \rfloor_{3,3} = \frac{J_{2,2}}{J_{2,2}J_{3,3}-J_{2,3}J_{3,2}}. \tag{32}$$

These three expressions would remain the same whether σ^2 is prior known or unknown. For the detailed expressions of $J_{1,1}, J_{2,2}, J_{2,3}, J_{3,2}$, and $J_{3,3}$, please refer to the Appendix.

To convert $\mathrm{CRB}_{\breve{R}_{\mathrm{LOS}}}$ of Eq. (32) to $\mathrm{CRB}_{R_{\mathrm{LOS}}}$, form $\theta' = [\phi, \psi, R_{\mathrm{LOS}}, \sigma^2]^T$ to give

$$\mathbf{J}(\theta')=\begin{bmatrix} J_{1,1} & 0 & 0 & 0 \\ 0 & J_{2,2} & kJ_{2,3} & 0 \\ 0 & kJ_{3,2} & k^2J_{3,3} & 0 \\ 0 & 0 & 0 & J_{4,4} \end{bmatrix}, \tag{33}$$

leading to

$$\begin{aligned}\mathrm{CRB}_{R_{\mathrm{LOS}}} &= \lfloor \mathbf{J}^{-1}(\theta') \rfloor_{3,3} = \frac{J_{2,2}}{k^2J_{2,2}J_{3,3}-k^2J_{2,3}J_{3,2}} \\ &= k^{-2}\mathrm{CRB}_{\breve{R}_{\mathrm{LOS}}}\left(\kappa,\ \psi,\ \breve{R}_{\mathrm{LOS}},\ \breve{D},\ \rho_0 c,\ \frac{\sigma^2}{2M}\right).\end{aligned} \tag{34}$$

The above Cramér-Rao bounds in Eqs. (30), (31), and (34) apply to any planar boundary. Section IV A–IV C will examine more closely the important special cases of a perfect-reflection boundary, a pressure-release boundary, and no boundary.

A. Special case #1 ($\kappa=\pm1$, $R_{\mathrm{LOS}}\to\infty$): CRB for a far-field source incident upon an AVS located near a perfect-reflection boundary or near a pressure-release boundary

As $R_{\mathrm{LOS}} \to \infty$, it follows that $\breve{R}_{\mathrm{LOS}}/\breve{R}_{\mathrm{re}} \to 1$ and $\delta = \breve{R}_{\mathrm{LOS}} - \breve{R}_{\mathrm{re}} \to -2\breve{D}\sin\psi$.[8] Consequently

$$J_{1,1} \to \frac{4M}{\sigma^2}\left[1+\kappa\cos\left(2\breve{D}\sin\psi\right)\right]\cos^2\psi, \tag{35}$$

$$\begin{aligned}J_{2,2} \to \frac{4M}{\sigma^2}\Big[&1-\kappa\cos(2\psi)\cos\left(2\breve{D}\sin\psi\right) \\ &+2\kappa\breve{D}\cos(\psi)\sin(2\psi)\sin\left(2\breve{D}\sin\psi\right) \\ &+2\breve{D}^2\left(1+(\rho_0 c)^2\right)\cos^2\psi\Big],\end{aligned} \tag{36}$$

$$J_{2,3} \to 0, \tag{37}$$

$$J_{3,3} \to 0. \tag{38}$$

The inverses of Eqs. (35) and (36) give the following CRB expressions for the far-field case with a perfect-reflection boundary or a pressure-release boundary:

$$\mathrm{CRB}_{\phi} = \frac{\sigma^2}{4M}\left\{\left[1+\kappa\cos\left(2\breve{D}\sin\psi\right)\right]\cos^2\psi\right\}^{-1}, \tag{39}$$

$$\begin{aligned}\mathrm{CRB}_{\psi} = \frac{\sigma^2}{4M}\Big\{&1-\kappa\cos(2\psi)\cos\left(2\breve{D}\sin\psi\right) \\ &+2\kappa\breve{D}\cos(\psi)\sin(2\psi)\sin\left(2\breve{D}\sin\psi\right) \\ &+2\breve{D}^2\left(1+(\rho_0 c)^2\right)\cos^2\psi\Big\}^{-1}.\end{aligned} \tag{40}$$

The above Eqs. (39) and (40) are consistent with the results in Ahmadi-Shokouh and Keshavarz (2007), by inverting the (2,2)th and (1,1)th entry of the $\mathbf{J}_w^{(x+y+z+p)}$ matrix in Appendix I-D there, by setting $R=1$, and by normalizing $\rho_0 c$ to unity.

B. Special case #2 ($\kappa=0$, $R_{\mathrm{LOS}}\to\infty$): CRB for a far-field source incident upon an AVS located near no boundary

Setting $R_{\mathrm{LOS}} \to \infty$ in Eqs. (43), (44), and (45), the far-field no-boundary case has the following closed-form CRB expressions:

$$\mathrm{CRB}_{\phi} = \frac{\sigma^2}{2M\cos^2\psi}, \tag{41}$$

$$\mathrm{CRB}_{\psi} = \frac{\sigma^2}{2M}. \tag{42}$$

There is no $\mathrm{CRB}_{R_{\mathrm{LOS}}}$ for this degenerate case, because $R_{\mathrm{LOS}} \to \infty$.

The above Eqs. (41) and (42) are compatible with Eq. (4.4) of Nehorai and Paldi (1994).

C. Special case #3 ($\kappa=0$): CRB for a not-necessarily-far-field source incident upon an AVS located near no boundary

The absence of any boundary means $\kappa = 0$ in Eqs. (30), (31), and (34). Then, together with Eqs. (A1), (A2), (A3), and (A4), the not-necessarily-far-field no-boundary case has the following closed-form CRB expressions:

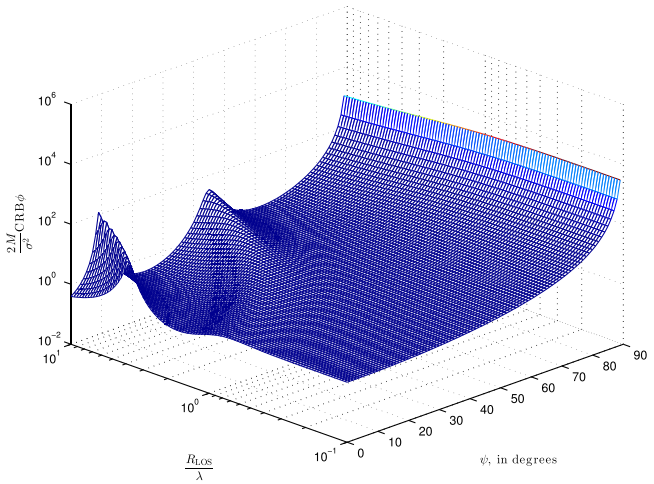

FIG. 4. (Color online) $2M/\sigma^2\,\mathrm{CRB}_\phi$ versus R_{LOS}/λ and ψ, at $D/\lambda = 1$.

$$\mathrm{CRB}_\phi = \frac{\sigma^2}{2M\,\cos^2\psi}, \tag{43}$$

$$\mathrm{CRB}_\psi = \frac{\sigma^2}{2M}, \tag{44}$$

$$\mathrm{CRB}_{R_{\mathrm{LOS}}} = \frac{\sigma^2}{2M}\left(\frac{1+k^2R_{\mathrm{LOS}}^2}{k\rho_0 c}\right)^2. \tag{45}$$

The above three expressions are compatible, respectively, to Eqs. (31), (32), and inverse of Eq. (23) of Wu *et al.* (2010), though a different data model was used in Wu *et al.* (2010).

V. QUALITATIVE OBSERVATIONS ON THE CRAMÉR-RAO BOUND FOR AN ACOUSTIC VECTOR-SENSOR NEAR A *PERFECT-REFLECTION* BOUNDARY

For a perfect-reflection boundary (i.e., $\kappa = 1$), Figs. 4–12 plot CRB_ϕ, CRB_ψ, or $\mathrm{CRB}_{R_{\mathrm{LOS}}}$—versus the parameters of ψ, R_{LOS}, or D, with $\rho_0 c$ normalized to unity for the pressure-sensor, as in Nehorai and Paldi (1994), Hawkes and Nehorai (2000), Ahmadi-Shokouh and Keshavarz (2007), Li *et al.* (2011), and Yuan (2012).

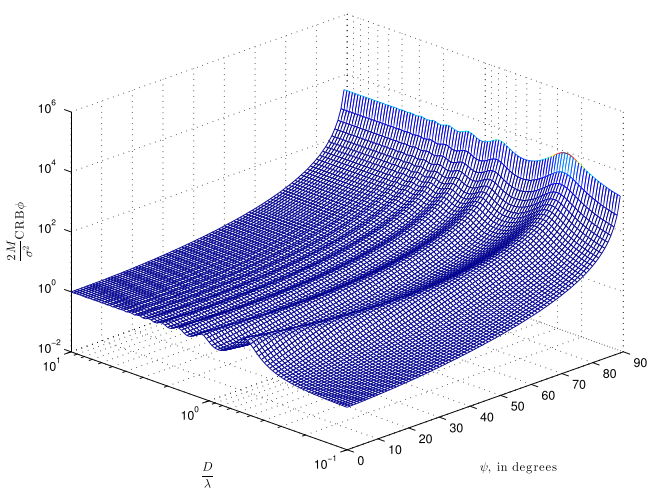

FIG. 5. (Color online) $2M/\sigma^2\,\mathrm{CRB}_\phi$ versus ψ and D/λ, at $R_{\mathrm{LOS}}/\lambda = 1$.

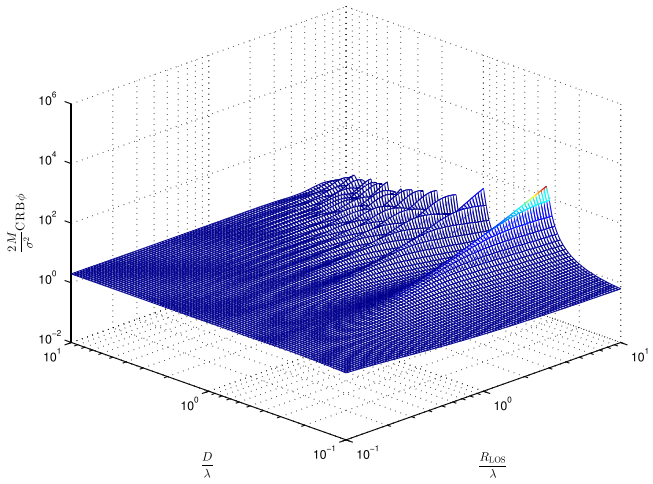

FIG. 6. (Color online) $2M/\sigma^2\,\mathrm{CRB}_\phi$ versus R_{LOS}/λ and D/λ, at $\psi = 45°$.

This paper's lack of space precludes the inclusion of figures for the pressure-release boundary case, which exhibits trends similar to those described/explained below for the perfect-reflection boundary case. This similarity is reasonable, as these two cases differ only in the sign (k) of the reflected wave's phase, which does not fundamentally alter the qualitative trends that will be described/explained below.

A. Observations on CRB_ϕ

Figures 4–6 plot $2M/\sigma^2\mathrm{CRB}_\phi$ versus ψ, R_{LOS}/λ, and D/λ. The following qualitative observations are made thereof:

(i) CRB_ϕ is independent of ϕ, as indicated in Eq. (30). This independence is expected, because $\hat{\phi}$ relies only on the projection of the incident wave (whether directly from the emitter or indirectly via the image source) onto the $x-y$ plane, and this projected wave power is independent of ϕ.

(ii) In Fig. 4 where $R_{\mathrm{LOS}}/\lambda \leq 1$ (i.e., outside the far field) and in Fig. 5, CRB_ϕ increases as ψ increases, due to the $\cos^{-2}(\psi)$ factor in Eq. (30). This is intuitively reasonable: As the emitter's direction-of-arrival

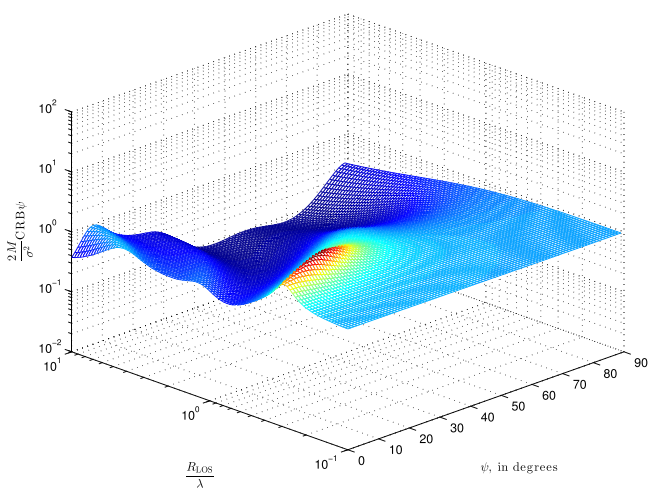

FIG. 7. (Color online) $2M/\sigma^2\,\mathrm{CRB}_\psi$ versus R_{LOS}/λ and ψ, at $D/\lambda = 1$.

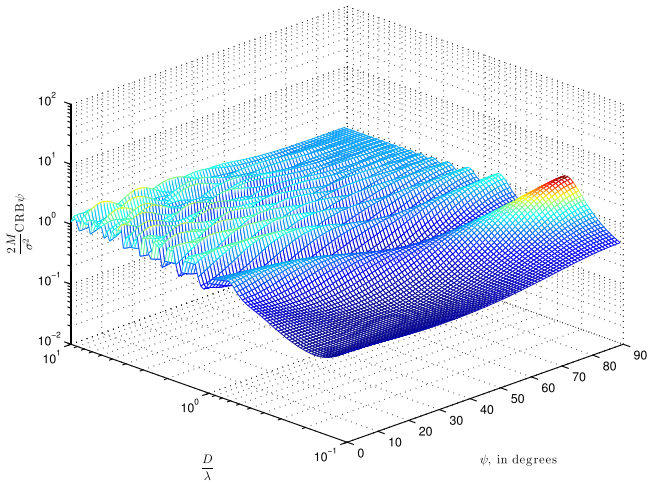

FIG. 8. (Color online) $2M/\sigma^2\,\mathrm{CRB}_\psi$ versus ψ and D/λ, at $R_{\mathrm{LOS}}/\lambda = 1$.

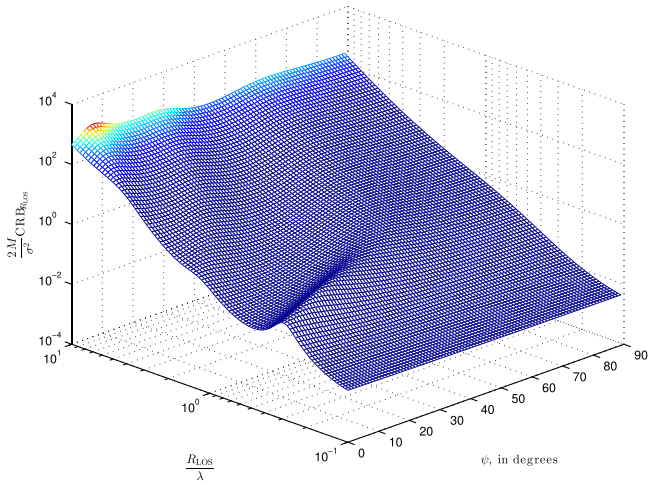

FIG. 10. (Color online) $2M/\sigma^2\,\mathrm{CRB}_{R_{\mathrm{LOS}}}$ versus R_{LOS}/λ and ψ, at $D/\lambda = 1$.

becomes more aligned with the vertical z axis (i.e., as $\psi \to \pi/2$), less of the incident energy will project onto the horizontal $x-y$ plane for the estimation of ϕ, hence a larger CRB_ϕ.

(iii) In Fig. 4 where $R_{\mathrm{LOS}}/\lambda > 1$ (i.e., outside the near field), CRB_ϕ generally increases as ψ increases, but not monotonically. "Ripples" arise, on account of $\cos(\delta)$ and $\sin(\delta)$, which become more influential in Eq. (30) at larger values of R_{LOS}/λ. Indeed, as $R_{\mathrm{LOS}} \to \infty$, Eq. (30) approaches Eq. (39), in which $\cos(2\breve{D}\sin\psi)$ may be expressed (via the Fourier series) as

$$\cos(2\breve{D}\sin\psi) = B_0(2\breve{D}) + 2\sum_{n=1}^{+\infty} B_{2n}(2\breve{D})\cos(2n\psi),$$

with B_i denoting the ith-order Bessel function of the first kind. That is, Eq. (30) implicitly involves a weighted sum of the monochromatic components $\cos(2n\psi)$, thereby explaining the ripples in Fig. 4.

(iv) Further consider the ripples in Figs. 4–6. Those ripples become lower but more frequent, as D/λ increases. This is intuitively reasonable: A larger D implies a weaker reflected wave, but affords more values of ψ at which the reflected wave and the LOS wave are in-phase (i.e., a ripple's crest) or anti-phase (i.e., a ripple's trough).

(v) Figure 6 is largely flat over D, at $R_{\mathrm{LOS}}/\lambda \le 1$ (i.e., outside the far field), where a short LOS propagation-path (therefore a strong LOS wave) dominates a reflected propagation-path that is proportionately much longer (thus a much weaker reflected wave). In contrast, at $R_{\mathrm{LOS}}/\lambda > 1$ (i.e., in the far field), CRB_ϕ is critically influenced by D; this is expected because a less dominant LOS wave is more vulnerable to constructive/destructive superposition with a reflected wave of more comparable power (because of a length ratio closer to 1).

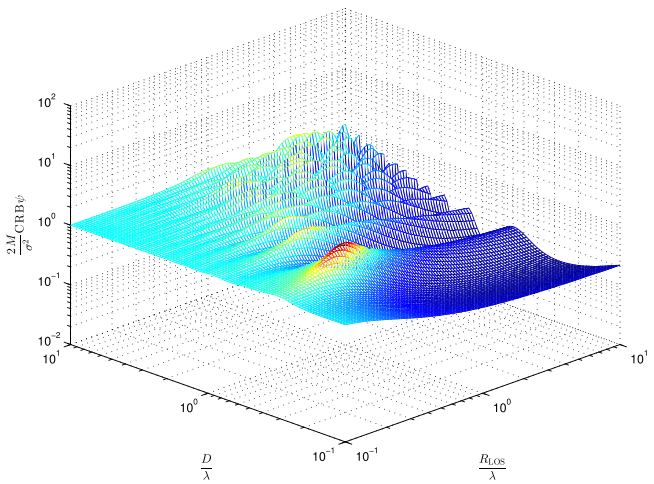

FIG. 9. (Color online) $2M/\sigma^2\,\mathrm{CRB}_\psi$ versus R_{LOS}/λ and D/λ, at $\psi = 45°$.

B. Observations on CRB_ψ

Figures 7–9 plot $2M/\sigma^2\mathrm{CRB}_\psi$, versus ψ, R_{LOS}/λ, and D/λ. From these figures, the following qualitative observations may be made:

(vi) CRB_ψ is independent of ϕ, as indeed required by Eq. (31).

(vii) CRB_ψ depends on ψ, unlike the far-field *no*-boundary case in Eq. (42) and unlike the not-necessarily-far-field *no*-boundary case in Eq. (44). This present dependency may be intuitively understood as follows: ψ affects the relative phases between the LOS wave and the reflected wave. As D/λ increases and as R_{LOS}/λ decreases, the reflected wave's propagation distance (in terms of the LOS wave's propagation distance) lengthens; therefore, the reflected wave weakens (relative to the LOS wave) and becomes dominated by the LOS wave, thereby diminishing the effects of ψ on CRB_ψ. This phenomenon also explains the flatness in Figs. 7 and 9, where R_{LOS}/λ is small and D/λ is large. (Asymptotically as $D/\lambda \to \infty$, the no-boundary case is obtained.)

(viii) Complementary to observation (vii) above: If the reflected wave is not negligible, CRB_ψ varies

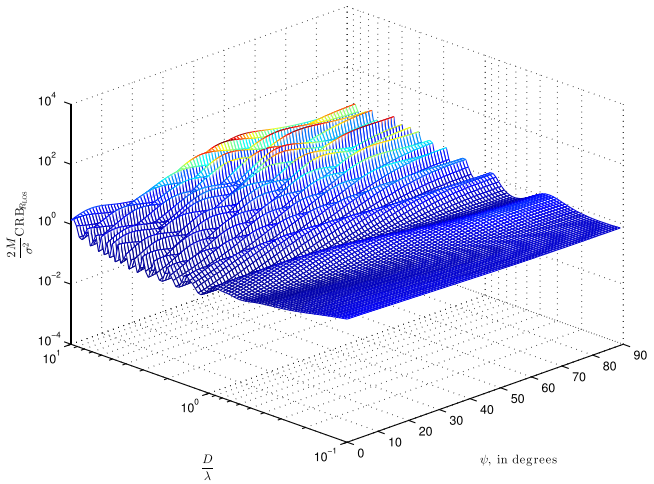

FIG. 11. (Color online) $2M/\sigma^2\,\mathrm{CRB}_{R_{\mathrm{LOS}}}$ versus ψ and D/λ, at $R_{\mathrm{LOS}}/\lambda = 1$.

significantly with ψ. Figure 7 shows that as R_{LOS}/λ increases, CRB_{ψ} would oscillate with ψ. Intuitively speaking: recall that the reflected wave here sums constructively/destructively with the LOS wave, to give the overall signal at the receiver; this constructive/destructive summation depends on the relative phase between the LOS wave and the reflected wave; and this relative phase varies with R_{LOS}/λ.

(ix) In Fig. 8, CRB_{ψ} oscillates with D/λ, which determines the extent of constructive-versus-destructive summation between the LOS wave and the reflected wave. The above-mentioned oscillation generally increases in amplitude, as R_{LOS}/λ increases, because a larger R_{LOS}/λ would cause the reflected wave's power to approximate the LOS wave's power, thereby magnifying the constructive/destructive summation effects.

(x) In Fig. 9 at a fixed D/λ, CRB_{ψ} generally decreases with an increasing R_{LOS}/λ, though not monotonically so. This is intuitively reasonable: A larger R_{LOS}/λ would imply greater proximity to unity for the ratio between the LOS distance versus the reflected wave's propagation distance. This means more comparable levels in power between the two waves at the acoustic vector-sensor, resulting in more pronounced effects from constructive/destructive summation.

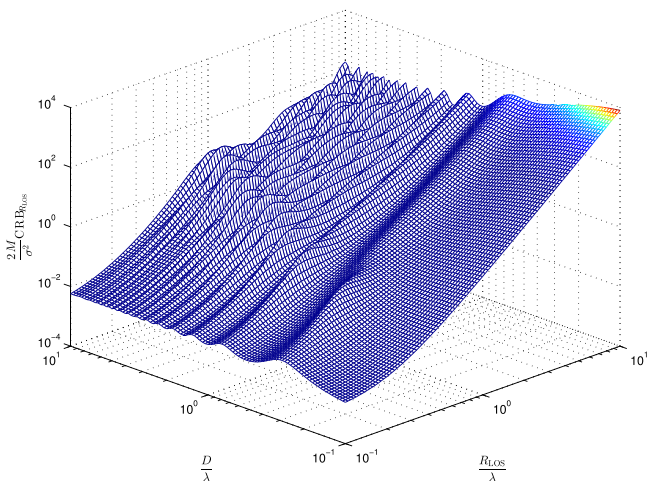

FIG. 12. (Color online) $2M/\sigma^2\,\mathrm{CRB}_{R_{\mathrm{LOS}}}$ versus R_{LOS}/λ and D/λ, at $\psi = 45°$.

C. Observations on $\mathrm{CRB}_{R_{\mathrm{LOS}}}$

Figures 10–12 plot $2M/\sigma^2\,\mathrm{CRB}_{R_{\mathrm{LOS}}}$ versus the parameters of ψ, R_{LOS}/λ and D/λ. The following qualitative observations may be made:

(xi) $\mathrm{CRB}_{R_{\mathrm{LOS}}}$ is independent of ϕ, as stipulated in Eq. (34).

(xii) From Figs. 10 and 12: $\mathrm{CRB}_{R_{\mathrm{LOS}}}$ generally increases with R_{LOS}/λ. This trend is similar to the not-necessarily-far-field *no*-boundary case. This is intuitively reasonable, because as R_{LOS}/λ increases, the estimate's resolution in R_{LOS}/λ would decrease, resulting in a larger $\mathrm{CRB}_{R_{\mathrm{LOS}}}$.

(xiii) Figures 10–12 together show that $\mathrm{CRB}_{R_{\mathrm{LOS}}}$ generally depends much more on R_{LOS}/λ, than on D/λ or ψ.

(xiv) Despite the previous observation in (xiii), $\mathrm{CRB}_{R_{\mathrm{LOS}}}$ does depend on D/λ and ψ, which affect the relative phase between the LOS wave and the reflected wave, hence their constructive/destructive summation. This effect shows up as the ripples in the figures.

VI. MAXIMUM-LIKELIHOOD DIRECTION FINDING OF A NEAR-FIELD EMITTER LYING NEAR A RIGID BOUNDARY

To demonstrate the significance of the array manifold presented in Sec. II, this section will investigate this array manifold's role in the maximum likelihood estimation (MLE) of a not-necessarily-far-field near-boundary emitter's azimuth-elevation arrival angle. This section will also show what could happen if this not-necessarily-far-field near-boundary array manifold were unavailable to the signal-processing algorithm-development engineer.[9]

Consider the scenario in Fig. 1, which relates a point-size emitter, an acoustic vector-sensor, and a rigid planar boundary. Suppose the signal-and-noise scenario is as described in Sec. IV, specifically in Eq. (27). Assuming that the signal-processing algorithm-development engineer knows of Eq. (19) after reading this paper, the maximum-likelihood estimate of (ϕ, ψ) would be constructed as

$$(\hat{\phi}, \hat{\psi}) = \underset{(\phi,\psi)}{\arg\max}\ \mathcal{L}, \tag{46}$$

where $\mathcal{L}$ denotes the log-likelihood function

$$\mathcal{L} = \sum_{m=1}^{M} \ln f\,(\tilde{\mathbf{z}}(m)|\phi, \psi), \tag{47}$$

with M referring to the total number of snapshots observed, and

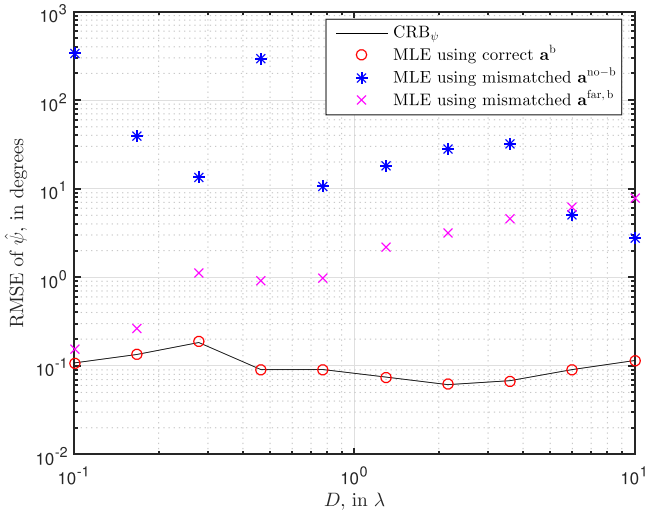

FIG. 13. (Color online) MLE of $\hat{\psi}$ versus CRB$_\psi$, at $(\phi, \psi, R_{\mathrm{LOS}}/\lambda) = (131°, 76°, 5)$, signal-to-noise ratio (SNR) = 20 dB, $M = 500$ time samples. There exist 5000 independent Monte Carlo experiments for each icon.

$$\ln f(\tilde{\mathbf{z}}(m)|\phi,\psi) = -\frac{1}{2}\left[4\ln(2\pi) + 4\ln(\sigma^2)\right] - \frac{1}{2\sigma^2}(\tilde{\mathbf{z}}(m)-\mu)^T(\tilde{\mathbf{z}}(m)-\mu),$$

$$\mu = \mathbf{a}^{(\mathrm{rigid})}s(mT_s).$$

Figures 13–16, by their "o" icons, indicate the maximum likelihood estimates obtained by presuming this availability of the not-necessarily-far-field near-rigid-boundary array manifold of Eq. (19). These estimates are very close to (visually coincide with) the Cramér-Rao bounds derived in Sec. IV, as would be expected.

In contrast, what if the signal-processing algorithm-development engineer has *no* knowledge of the not-necessarily-far-field near-rigid-boundary array manifold of Eq. (19) presented in this paper?

(A) Suppose he/she then mistakenly uses the far-field near-rigid-boundary array manifold of Eq. (21) in which $\Gamma_p(\psi,\omega) = 1$, thereby mistaking $\boldsymbol{\mu}$ as

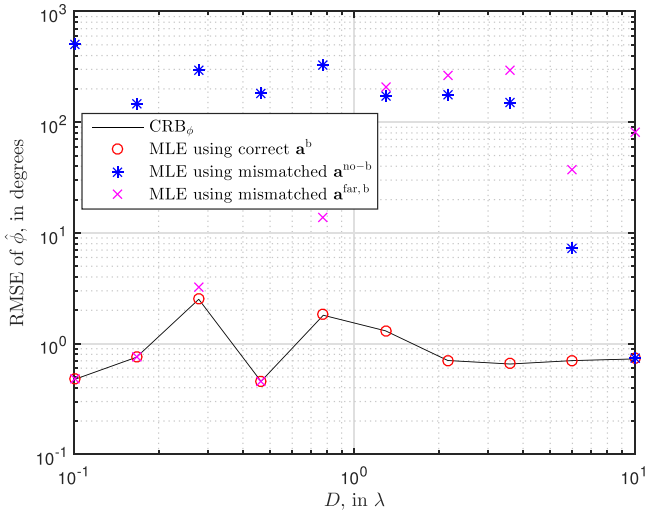

FIG. 14. (Color online) MLE of $\hat{\phi}$ versus CRB$_\phi$, at $(\phi, \psi, R_{\mathrm{LOS}}/\lambda) = (131°, 76°, 5)$, SNR = 20 dB, $M = 500$ time samples. There exist 5000 independent Monte Carlo experiments for each icon.

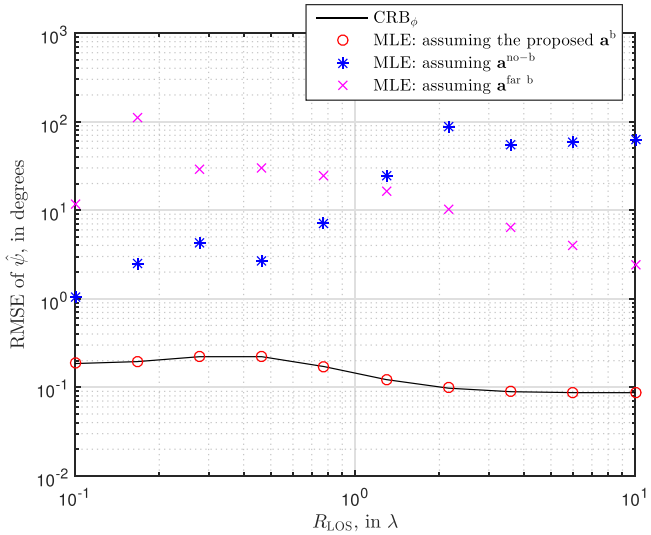

FIG. 15. (Color online) MLE of $\hat{\psi}$ versus CRB$_\psi$, at $(\phi, \psi, D/\lambda) = (58°, 25°, 0.5)$, SNR = 20 dB, $M = 500$ time samples. There exist 5000 independent Monte Carlo experiments for each icon.

$$\boldsymbol{\mu}^{(\mathrm{far,b})} = \mathbf{a}^{(\mathrm{far,b})}s(mTs). \tag{48}$$

(B) Or, suppose he/she mistakenly uses the no-boundary array manifold of Eq. (22), thereby mistaking $\boldsymbol{\mu}$ as

$$\boldsymbol{\mu}^{(\mathrm{no-b})} = \mathbf{a}^{(\mathrm{no-b})}s(mTs). \tag{49}$$

Figures 13–16 use the "x" icons to indicate the estimates based on the mismatched case of (A), whereas the "*" icons indicate the estimates of the mismatched case of (B). These figures show that the model-mismatched cases can increase the estimation error, sometimes by many multiples or even by orders-of-magnitude. Hence, the algorithm should always use the array manifold derived in Sec. II, which is applicable to the general scenario whether far-field or near-field, whether near a boundary or not near any boundary (i.e., for $D/\lambda \to \infty$).

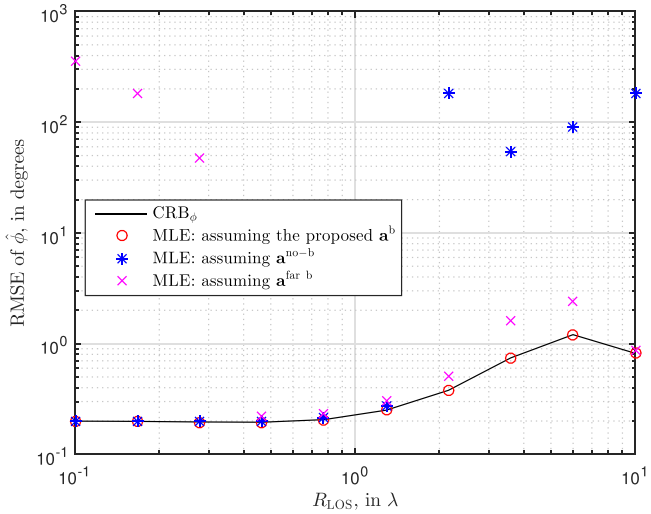

FIG. 16. (Color online) MLE of $\hat{\phi}$ versus CRB$_\phi$, at $(\phi, \psi, D/\lambda) = (58°, 25°, 0.5)$, SNR = 20 dB, $M = 500$ time samples. There exist 5000 independent Monte Carlo experiments for each icon.

The following qualitative observations may be made in Figs. 13–16:

(xv) The "far, b" model mismatch would lessen, if either
  (xv-1) D/λ decreases beyond $D/\lambda \ll 1$ (at the constant $R_{\mathrm{LOS}}/\lambda = 5$ in Figs. 13 and 14), or
  (xv-2) R_{LOS}/λ increases (at the constant $D/\lambda = 1/2$ in Figs. 15 and 16).

(xvi) The no-b model mismatch would lessen, if either
  (xvi-1) D/λ increases toward 10 (at the constant $R_{\mathrm{LOS}}/\lambda = 5$ in Figs. 13 and 14), or
  (xvi-2) R_{LOS}/λ decreases beyond $R_{\mathrm{LOS}}/\lambda \ll 1$ (at the constant $D/\lambda = 1/2$ in Figs. 15 and 16).

The above graphical trends result from the superposition between the two waves—the direct LOS wave and the reflected wave. Specifically, these two waves' constructive-versus-destructive summation is determined by their relative complex-phase and relative magnitude:

(a) The two waves' complex phases would approximate each other, if $D/\lambda \ll 1$. Moreover, these two complex phases would more closely approach each other, as D/λ decreases further toward zero.

(b) Recall that the array manifold presented in Sec. II accounts for propagation path loss. Hence, if the two waves' propagation distances approximate each other (e.g., if $R_{\mathrm{LOS}}/\lambda \gg D/\lambda$), the two waves' magnitudes would approximate each other, thereby facilitating a possibly severe destructive summation.

How may points (a) and (b) explain the graphical trends of (xv) and (xvi)?

Trend (xv-1) may be explained by (a): Constructive summation dominates at $D/\lambda \ll 1$, thereby tending to "merge" the two waves into one, whether the emitter lies in the far field or not. This "merging" approaches perfect constructive summation as $D/\lambda \to 0$.

Trend (xv-2) may be explained as follows: The no-b model represents simply a degeneration of the b model as $D/\lambda \to \infty$.

Trend (xvi-1) may be explained by (a), because the reflected wave becomes very weak, hence increasingly negligible.

Trend (xvi-2) may be explained by (b): As R_{LOS}/λ, already below $2(\mathrm{D}/\lambda)$, keeps getting shorter: the direct LOS wave has a propagation path progressively shorter than the reflected wave's, thus an increasingly dominant magnitude. This renders the reflected wave increasingly negligible in any constructive/destructive summation with the direct LOS wave.

VII. IMPLICATIONS ON THE SPATIAL RESOLUTION BETWEEN TWO CLOSELY SPACED EMITTERS

The analysis in the preceding Secs. IV–VI has dealt with a single incident emitter. If there exist two emitters, how spatially nearby may they be to each other but still remain resolvable, according to the array manifold in Eq. (19) for a rigid planar boundary?

More mathematically, consider a two-source scenario where the data equals

$$\breve{\mathbf{z}} = \underbrace{\mathbf{s}_1 \otimes \mathbf{a}_\kappa(\phi_1,\psi_1,R_{1,\mathrm{LOS}}) + \mathbf{s}_2 \otimes \mathbf{a}_\kappa(\phi_2,\psi_2,R_{2,\mathrm{LOS}})}_{=\mu_2} + \tilde{\mathbf{n}}. \tag{50}$$

The above expression follows the notational style in Eq. (27), with the subscripts of $_1$ and $_2$ indexing the incident sources, e.g., $\mathbf{s}_1 = \mathrm{e}^{\mathrm{j}\epsilon_1}[\mathrm{e}^{\mathrm{j}T_s\omega}, \mathrm{e}^{\mathrm{j}2T_s\omega}, \ldots, \mathrm{e}^{\mathrm{j}MT_s\omega}]^T$ and $\mathbf{s}_2 = \mathrm{e}^{\mathrm{j}\epsilon_2}[\mathrm{e}^{\mathrm{j}T_s\omega}, \mathrm{e}^{\mathrm{j}2T_s\omega}, \ldots, \mathrm{e}^{\mathrm{j}MT_s\omega}]^T$.

Now, the unknown entities are 7 in number: ϕ_1, ψ_1, $R_{1,\mathrm{LOS}}$, ϕ_2, ψ_2, $R_{2,\mathrm{LOS}}$, σ^2; and the FIM of Eq. (29) becomes 7×7 in size.

Measure the direction-finding error for the ith source via the scalar metric of

$$\vartheta_i = \cos^{-1}\left(\begin{bmatrix} \cos(\phi_i)\cos(\psi_i) \\ \sin(\phi_i)\cos(\psi_i) \\ \sin(\psi_i) \end{bmatrix} \cdot \begin{bmatrix} \cos(\hat{\phi}_i)\cos(\hat{\psi}_i) \\ \sin(\hat{\phi}_i)\cos(\hat{\psi}_i) \\ \sin(\hat{\psi}_i) \end{bmatrix} \right), \tag{51}$$

where $\cdot$ refers to the inner product between two vectors. The corresponding mean-square angular error (MSAE), $E\{\vartheta_i^2\}$, is lower bounded by Nehorai and Hawkes (2000) as

$$\mathrm{MSAE}_i^{(\mathrm{LB})} = \cos^2(\psi_i)\,\mathrm{CRB}_{\phi_i} + \mathrm{CRB}_{\psi_i}. \tag{52}$$

A. Scenario #1

Two incident sources have $\phi_1 = 15°$, $\phi_2 = 71°$, $\psi_1 = \psi_2 = 43°$, $\omega = 2\pi\,\mathrm{kHz}$, $\epsilon_1 = 0$, and $\epsilon_2 = 0.17\pi$.[10] Hence, these two sources would differ spatially only in their incident azimuth angles.

Figure 17 plots $\mathrm{MSAE}_1^{(\mathrm{LB})} + \mathrm{MSAE}_2^{(\mathrm{LB})}$ versus D/λ and versus $R_{1,\mathrm{LOS}} = R_{2,\mathrm{LOS}}$. As $R_{1,\mathrm{LOS}} = R_{2,\mathrm{LOS}}$ decreases, the two sources traverse from the far field into the near field, thus their Cartesian separation shrinks, yet $\mathrm{MSAE}_1^{(\mathrm{LB})} + \mathrm{MSAE}_2^{(\mathrm{LB})}$ does

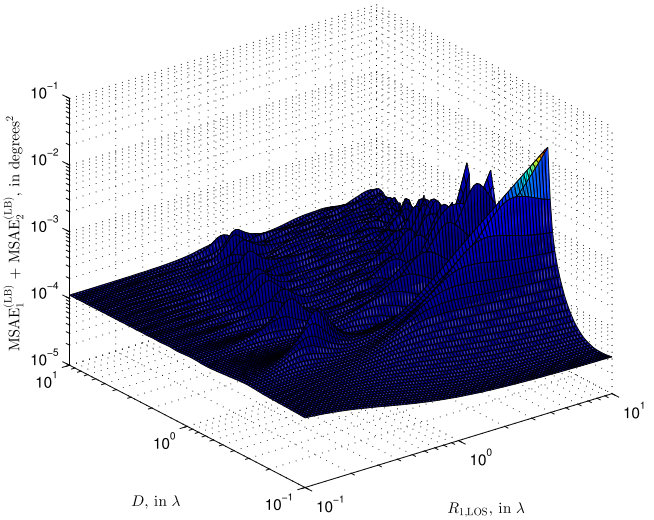

FIG. 17. (Color online) $\mathrm{MSAE}_1^{(\mathrm{LB})} + \mathrm{MSAE}_2^{(\mathrm{LB})}$, against $R_{1,\mathrm{LOS}} = R_{2,\mathrm{LOS}}$ and D, at $(\phi_1, \phi_2, \psi_1, \psi_2) = (15°, 71°, 43°, 43°)$ and $\mathrm{SNR} = 20\,\mathrm{dB}$.

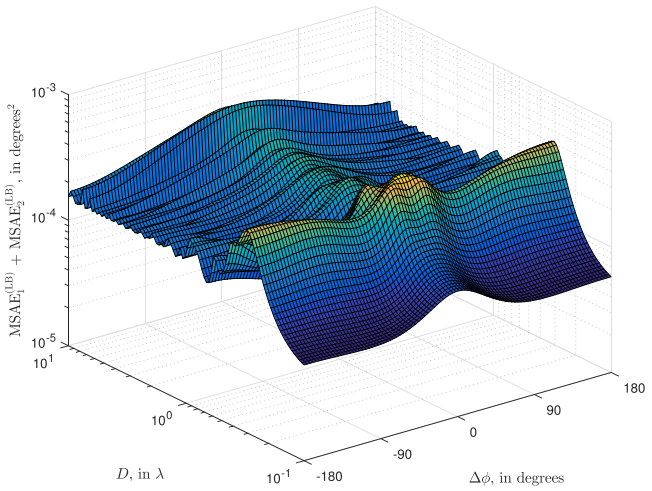

FIG. 18. (Color online) $\mathrm{MSAE}_1^{(\mathrm{LB})} + \mathrm{MSAE}_2^{(\mathrm{LB})}$, against $\Delta\phi$ and D, at $(\phi_1, \phi_2, \psi_1, \psi_2, R_{1,\mathrm{LOS}}, R_{1,\mathrm{LOS}}) = (74°, 74° + \Delta\phi, 43°, 43°, 1\lambda, 1\lambda)$ and $\mathrm{SNR} = 20\,\mathrm{dB}$.

not increase significantly. This counter-intuitive phenomenon could be explained by the stronger received signal level, due to less attenuation of the LOS wave. On the other hand, at large $R_{1,\mathrm{LOS}} = R_{2,\mathrm{LOS}}$, fluctuation arises over Δ/λ, due to echoes off the reflection boundary. Indeed, Fig. 17 shows many trends previously discussed in Figs. 6 and 9. This is expected, because the MSAE equals a weighted sum of CRB_ϕ and CRB_ψ.

B. Scenario #2

Now, the two incident sources have $\phi_1 = 74°$, $\phi_2 = \phi_1 + \Delta\phi$, $\psi_1 = \psi_2 = 43°$, $R_{1,\mathrm{LOS}} = R_{2,\mathrm{LOS}} = \lambda$, ω, $\omega = 2\pi$ kHz, $\epsilon_1 = 0$, and $\epsilon_1 = 0.13\pi$.[11] Hence, these two sources would also differ spatially only in their incident azimuth angles.

Figure 18 plots $\mathrm{MSAE}_1^{(\mathrm{LB})} + \mathrm{MSAE}_2^{(\mathrm{LB})}$ versus D/λ and versus $\Delta\phi$. There, $\mathrm{MSAE}_1^{(\mathrm{LB})} + \mathrm{MSAE}_2^{(\mathrm{LB})}$ is symmetric with respect to $\Delta\phi = 0°$. This symmetry is expected from Eq. (52) along with the earlier stated observations (i) and (vi), which together imply that $\mathrm{MSAE}_1^{(\mathrm{LB})} + \mathrm{MSAE}_2^{(\mathrm{LB})}$ is independent of ϕ. Moreover, at a constant D/λ, the graph generally becomes unimodal with respect to $\Delta\phi$, i.e., $\mathrm{MSAE}_1^{(\mathrm{LB})} + \mathrm{MSAE}_2^{(\mathrm{LB})}$ increases as $\Delta\phi \to 0°$.

This unimodality holds except for a small range of $D/\lambda \in [0.16, 0.56]$, on account of the reflected waves. At larger values of D/λ above unity, the effects of the reflected waves would lessen and unimodality would always hold. Furthermore, the graph fluctuates with D/λ, as observed similarly of $\mathrm{MSAE}_1^{(\mathrm{LB})}$ or $\mathrm{MSAE}_2^{(\mathrm{LB})}$, individually, in Secs. VII A. The reason is the same: due to echoes off the reflection boundary, as already discussed in an earlier section.

VIII. CONCLUSION

A measurement model is presented here for an acoustic vector-sensor located near a reflecting boundary, with the emitter lying in the near field, the far field, or anywhere in between. This measurement model is presented as a 4×1 array manifold vector that depends on the incident signal's frequency, on the boundary's reflection coefficient, as well as on the spatial geometry relating the acoustic vector-sensor, the emitter, and the boundary. The corresponding source-localization Cramér-Rao bounds are analytically derived. These Cramér-Rao bounds show the critical effects of the constructive/destruction summation between the LOS wave and the reflected wave. The algorithmic significance of this new array manifold is shown through a model-mismatched study wherein this new array manifold is unavailable. The spatial resolution in relation to two coexisting emitters is also investigated under this measurement model.

ACKNOWLEDGMENTS

The authors were supported by Grant no. PolyU-5271/12E and Grant no. PolyU-152172/14E from Hong Kong's Research Grants Council. The authors would like to thank Professor Finn Jacobsen and Professor Charles Hung Lee for useful discussions.

APPENDIX: CLOSED-FORM EXPRESSION FOR $J_{i,j}$

$$J_{1,1} = \frac{2M}{\sigma^2}\frac{\cos^2\psi}{\left(1+\breve{R}_{\mathrm{LOS}}^2\right)\breve{R}_{\mathrm{re}}^6}\Big[\kappa^2\breve{R}_{\mathrm{LOS}}^6 + \breve{R}_{\mathrm{re}}^6 + \breve{R}_{\mathrm{LOS}}^2\breve{R}_{\mathrm{re}}^2\left(\kappa^2\breve{R}_{\mathrm{LOS}}^4 + \breve{R}_{\mathrm{re}}^4\right) + 2\kappa\,\breve{R}_{\mathrm{LOS}}^3\breve{R}_{\mathrm{re}}^3\left(\breve{R}_{\mathrm{LOS}}\breve{R}_{\mathrm{re}} + 1\right)\cos(\delta) + 2\kappa\delta\,\breve{R}_{\mathrm{LOS}}^3\breve{R}_{\mathrm{re}}^3\sin(\delta)\Big], \tag{A1}$$

$$J_{1,2} = J_{1,3} = J_{1,4} = J_{2,1} = 0,$$

$$J_{2,2} = \frac{2M}{\sigma^2}\frac{1}{\left(1+\breve{R}_{\mathrm{LOS}}^2\right)\breve{R}_{\mathrm{re}}^{10}}\Big[C_{2,2}^{(1)} + C_{2,2}^{(4)}\cos(\delta) + C_{2,2}^{(6)}\sin(\delta) + \left(2C_{2,2}^{(5)}\cos(\delta) + 2C_{2,2}^{(7)}\sin(\delta) + C_{2,2}^{(9)}\right)\cos(2\psi) + 2\left(2C_{2,2}^{(2)}\cos(\delta) + 2C_{2,2}^{(3)}\sin(\delta) + C_{2,2}^{(8)}\right)\cos(\psi) \times \cos(\psi)\sin(2\psi)\Big], \tag{A2}$$

$$J_{2,3} = J_{3,2} = \frac{2M}{\sigma^2}\frac{\kappa\cdot\breve{R}_{\mathrm{LOS}}\cos\psi}{\left(1+\breve{R}_{\mathrm{LOS}}^2\right)^2\breve{R}_{\mathrm{re}}^{10}}\Big[C_{2,3}^{(1)} + C_{2,3}^{(4)}\cos(\delta) + C_{2,3}^{(5)}\sin(\delta) + \left(2C_{2,3}^{(2)}\cos(\delta) + 2C_{2,3}^{(3)}\sin(\delta) + C_{2,2}^{(8)}\right)\cos(2\psi) + 2\left(2C_{2,2}^{(6)}\cos(\delta) + 2C_{2,3}^{(7)}\sin(\delta) + C_{2,3}^{(9)}\right)\sin(\psi)\Big], \tag{A3}$$

$$J_{2,4} = J_{3,1} = 0,$$

$$J_{3,3} = \frac{2M}{\sigma^2}\frac{1}{\left(1+\breve{R}_{\mathrm{LOS}}^2\right)^2\breve{R}_{\mathrm{re}}^{10}}\Big[C_{3,3}^{(1)} + C_{3,3}^{(2)}\sin(\delta) + C_{3,3}^{(3)}\cos(\delta) + \left(-2C_{3,3}^{(4)}\sin(\delta) - 2C_{3,3}^{(5)}\cos(\delta) + C_{3,3}^{(7)}\right) \times \sin(\psi)C_{3,3}^{(8)}\cos(2\psi) + C_{3,3}^{(6)}\sin(3\psi)\Big], \tag{A4}$$

$$J_{3,4} = J_{4,1} = J_{4,2} = J_{4,3} = 0, \tag{A5}$$

$$J_{4,4} = \frac{4M}{\sigma^4}, \tag{A6}$$

with $\delta = \breve{R}_{\mathrm{LOS}} - \breve{R}_{\mathrm{re}}$.

Furthermore,

$$\begin{aligned}
C_{2,2}^{(1)} &= \breve{R}_{\mathrm{re}}^{10} + \breve{R}_{\mathrm{LOS}}^{2}\breve{R}_{\mathrm{re}}^{10} + \kappa^2(\breve{R}_{\mathrm{LOS}}^{6}\breve{R}_{\mathrm{re}}^{4} + \breve{R}_{\mathrm{LOS}}^{6}\breve{R}_{\mathrm{re}}^{6} + 18\breve{R}_{\mathrm{LOS}}^{8}\breve{D}^{2} - 12\breve{R}_{\mathrm{LOS}}^{6}\breve{R}_{\mathrm{re}}^{2}\breve{D}^{2} + 6\breve{R}_{\mathrm{LOS}}^{8}\breve{R}_{\mathrm{re}}^{2}\breve{D}^{2} \\
&\quad -8\breve{R}_{\mathrm{LOS}}^{6}\breve{R}_{\mathrm{re}}^{4}\breve{D}^{2} + 2(\rho_0 c)^2\breve{R}_{\mathrm{LOS}}^{6}\breve{R}_{\mathrm{re}}^{4}\breve{D}^{2} + 2\breve{R}_{\mathrm{LOS}}^{8}\breve{R}_{\mathrm{re}}^{4}\breve{D}^{2} + 2(\rho_0 c)^2\breve{R}_{\mathrm{LOS}}^{6}\breve{R}_{\mathrm{re}}^{6}\breve{D}^{2} + 72\breve{R}_{\mathrm{LOS}}^{6}\breve{D}^{4} \\
&\quad +24\breve{R}_{\mathrm{LOS}}^{6}\breve{R}_{\mathrm{re}}^{2}\breve{D}^{4} + 8\breve{R}_{\mathrm{LOS}}^{2}\breve{D}^{4} + 8R_{\mathrm{LOS}}^{6}\breve{R}_{\mathrm{re}}^{4}\breve{D}^{4}),
\end{aligned}$$

$$C_{2,2}^{(2)} = \kappa\breve{R}_{\mathrm{LOS}}^{4}\breve{R}_{\mathrm{re}}^{5}(3 + 3\breve{R}_{\mathrm{LOS}}\breve{R}_{\mathrm{re}} - \breve{R}_{\mathrm{re}}^{2})\breve{D},$$

$$C_{2,2}^{(3)} = -\kappa\breve{R}_{\mathrm{LOS}}^{4}\breve{R}_{\mathrm{re}}^{5}(-3\breve{R}_{\mathrm{LOS}} + 3\breve{R}_{\mathrm{re}} + \breve{R}_{\mathrm{LOS}}\breve{R}_{\mathrm{re}}^{2})\breve{D},$$

$$C_{2,2}^{(4)} = 4\kappa\breve{R}_{\mathrm{LOS}}^{3}\breve{R}_{\mathrm{re}}^{5}(3 + 3\breve{R}_{\mathrm{LOS}}\breve{R}_{\mathrm{re}} - \breve{R}_{\mathrm{re}}^{2})\breve{D}^{2},$$

$$C_{2,2}^{(5)} = -\kappa\breve{R}_{\mathrm{LOS}}^{3}\breve{R}_{\mathrm{re}}^{5}(\breve{R}_{\mathrm{re}}^{2} + \breve{R}_{\mathrm{LOS}}\breve{R}_{\mathrm{re}}^{3} - 6\breve{D}^{2} - 6\breve{R}_{\mathrm{LOS}}\breve{R}_{\mathrm{re}}^{2}\breve{D}^{2} + 2\breve{R}_{\mathrm{re}}^{2}\breve{D}^{2}),$$

$$C_{2,2}^{(6)} = -4\kappa\breve{R}_{\mathrm{LOS}}^{3}\breve{R}_{\mathrm{re}}^{5}(-3\breve{R}_{\mathrm{LOS}} + 3\breve{R}_{\mathrm{re}} + \breve{R}_{\mathrm{LOS}}\breve{R}_{\mathrm{re}}^{2})\breve{D}^{2},$$

$$C_{2,2}^{(7)} = -\kappa\breve{R}_{\mathrm{LOS}}^{3}\breve{R}_{\mathrm{re}}^{5}(\breve{R}_{\mathrm{LOS}}\breve{R}_{\mathrm{re}}^{2} - \breve{R}_{\mathrm{re}}^{3} - 6\breve{R}_{\mathrm{LOS}}\breve{D}^{2} + 6\breve{R}_{\mathrm{re}}\breve{D}^{2} + 2\breve{R}_{\mathrm{LOS}}\breve{R}_{\mathrm{re}}^{2}\breve{D}^{2}),$$

$$C_{2,2}^{(8)} = 4\kappa\breve{R}_{\mathrm{LOS}}^{7}(9 + 3\breve{R}_{\mathrm{re}} + \breve{R}_{\mathrm{re}}^{4})\breve{D}^{3},$$

$$\begin{aligned}
C_{2,2}^{(9)} &= 2\kappa\breve{R}_{\mathrm{LOS}}^{6}\breve{D}^{2}(9\breve{R}_{\mathrm{LOS}}^{2} - 6\breve{R}_{\mathrm{re}}^{2} + 3\breve{R}_{\mathrm{LOS}}^{2}\breve{R}_{\mathrm{re}}^{2} - 4\breve{R}_{\mathrm{re}}^{4} + (\rho_0 c)^2\breve{R}_{\mathrm{re}}^{4} + \breve{R}_{\mathrm{LOS}}^{2}\breve{R}_{\mathrm{re}}^{4} + (\rho_0 c)^2\breve{R}_{\mathrm{re}}^{6} \\
&\quad +36\breve{D}^{2} + 12\breve{R}_{\mathrm{re}}^{2}\breve{D}^{2} + 4\breve{R}_{\mathrm{re}}^{4}\breve{D}^{2})
\end{aligned}$$

$$\begin{aligned}
C_{2,3}^{(1)} &= 2\kappa\breve{R}_{\mathrm{LOS}}^{3}\breve{D}(9\breve{R}_{\mathrm{LOS}}^{4} + 9\breve{R}_{\mathrm{LOS}}^{6} - 12\breve{R}_{\mathrm{LOS}}^{2}\breve{R}_{\mathrm{re}}^{2} - 6\breve{R}_{\mathrm{LOS}}^{4}\breve{R}_{\mathrm{re}}^{2} + 3\breve{R}_{\mathrm{LOS}}^{6}\breve{R}_{\mathrm{re}}^{2} + 2\breve{R}_{\mathrm{re}}^{4} - 7\breve{R}_{\mathrm{LOS}}^{2}\breve{R}_{\mathrm{re}}^{2} \\
&\quad +(\rho_0 c)^2\breve{R}_{\mathrm{LOS}}^{2}\breve{R}_{\mathrm{re}}^{4} - 5\breve{R}_{\mathrm{LOS}}^{4}\breve{R}_{\mathrm{re}}^{4} + (\rho_0 c)^2\breve{R}_{\mathrm{LOS}}^{4}\breve{R}_{\mathrm{re}}^{4} + \breve{R}_{\mathrm{LOS}}^{6}\breve{R}_{\mathrm{re}}^{4} - \breve{R}_{\mathrm{LOS}}^{5}\breve{R}_{\mathrm{re}}^{5} + 2\breve{R}_{\mathrm{re}}^{6} - 2(\rho_0 c)^2\breve{R}_{\mathrm{re}}^{6} \\
&\quad +\breve{R}_{\mathrm{LOS}}^{2}\breve{R}_{\mathrm{re}}^{6} + (\rho_0 c)^2\breve{R}_{\mathrm{LOS}}^{4}\breve{R}_{\mathrm{re}}^{6} - (\rho_0 c)^2\breve{R}_{\mathrm{LOS}}^{3}\breve{R}_{\mathrm{re}}^{7} + 72\breve{R}_{\mathrm{LOS}}^{2}\breve{D}^{2} + 72\breve{R}_{\mathrm{LOS}}^{4}\breve{D}^{2} - 24\breve{R}_{\mathrm{re}}^{2}\breve{D}^{2} \\
&\quad +12\breve{R}_{\mathrm{LOS}}^{2}\breve{R}_{\mathrm{re}}^{2}\breve{D}^{2} + 24\breve{R}_{\mathrm{LOS}}^{4}\breve{R}_{\mathrm{re}}^{2}\breve{D}^{2} - 16\breve{R}_{\mathrm{re}}^{4}\breve{D}^{2} + 8\breve{R}_{\mathrm{LOS}}^{4}\breve{R}_{\mathrm{re}}^{4}\breve{D}^{2} - 4\breve{R}_{\mathrm{LOS}}^{3}\breve{R}_{\mathrm{re}}^{5}\breve{D}^{2}),
\end{aligned}$$

$$C_{2,3}^{(2)} = -\breve{R}_{\mathrm{LOS}}^{2}(1 + \breve{R}_{\mathrm{LOS}}^{2})\breve{R}_{\mathrm{re}}^{5}(3 + 3\breve{R}_{\mathrm{LOS}}\breve{R}_{\mathrm{re}} - \breve{R}_{\mathrm{re}}^{2})\breve{D},$$

$$C_{2,3}^{(3)} = \breve{R}_{\mathrm{LOS}}^{2}(1 + \breve{R}_{\mathrm{LOS}}^{2})\breve{R}_{\mathrm{re}}^{5}(-3\breve{R}_{\mathrm{LOS}} + 3\breve{R}_{\mathrm{re}} + \breve{R}_{\mathrm{LOS}}\breve{R}_{\mathrm{re}}^{2})\breve{D},$$

$$\begin{aligned}
C_{2,3}^{(4)} &= 2\breve{R}_{\mathrm{re}}^{5}(6\breve{R}_{\mathrm{LOS}}^{2} + 6\breve{R}_{\mathrm{LOS}}^{4} + 6\breve{R}_{\mathrm{LOS}}^{3}\breve{R}_{\mathrm{re}} + 6\breve{R}_{\mathrm{LOS}}^{5}\breve{R}_{\mathrm{re}} - 2\breve{R}_{\mathrm{re}}^{2} - 3\breve{R}_{\mathrm{LOS}}^{2}\breve{R}_{\mathrm{re}}^{2} - (\rho_0 c)^2\breve{R}_{\mathrm{LOS}}^{2}\breve{R}_{\mathrm{re}}^{2} \\
&\quad -3\breve{R}_{\mathrm{LOS}}^{4}\breve{R}_{\mathrm{re}}^{2} - 2\breve{R}_{\mathrm{LOS}}\breve{R}_{\mathrm{re}}^{3} + (\rho_0 c)^2\breve{R}_{\mathrm{LOS}}^{3}\breve{R}_{\mathrm{re}}^{3})\,\breve{D},
\end{aligned}$$

$$\begin{aligned}
C_{2,3}^{(5)} &= -2\breve{R}_{\mathrm{re}}^{5}(-6\breve{R}_{\mathrm{LOS}}^{3} - 6\breve{R}_{\mathrm{LOS}}^{5} + 6\breve{R}_{\mathrm{LOS}}^{2}\breve{R}_{\mathrm{re}} + 6\breve{R}_{\mathrm{LOS}}^{4}\breve{R}_{\mathrm{re}} + 2\breve{R}_{\mathrm{LOS}}\breve{R}_{\mathrm{re}}^{2} + \breve{R}_{\mathrm{LOS}}^{3}\breve{R}_{\mathrm{re}}^{2} \\
&\quad -(\rho_0 c)^2\breve{R}_{\mathrm{LOS}}^{3}\breve{R}_{\mathrm{re}}^{2} - 2\breve{R}_{\mathrm{re}}^{3} + 2\breve{R}_{\mathrm{LOS}}^{5}\breve{R}_{\mathrm{re}}^{2} - \breve{R}_{\mathrm{LOS}}^{2}\breve{R}_{\mathrm{re}}^{3} - (\rho_0 c)^2\breve{R}_{\mathrm{LOS}}^{2}\breve{R}_{\mathrm{re}}^{3} - \breve{R}_{\mathrm{LOS}}^{4}\breve{R}_{\mathrm{re}}^{3})\,\breve{D},
\end{aligned}$$

$$\begin{aligned}
C_{2,3}^{(6)} &= \breve{R}_{\mathrm{LOS}}\breve{R}_{\mathrm{re}}^{5}(3\breve{R}_{\mathrm{LOS}}^{2} + 3\breve{R}_{\mathrm{LOS}}^{4} + 3\breve{R}_{\mathrm{LOS}}^{3}\breve{R}_{\mathrm{re}} + 3\breve{R}_{\mathrm{LOS}}^{5}\breve{R}_{\mathrm{re}} - 3\breve{R}_{\mathrm{re}}^{2} - 3\breve{R}_{\mathrm{LOS}}^{2}\breve{R}_{\mathrm{re}}^{2} - 2\breve{R}_{\mathrm{LOS}}^{4}\breve{R}_{\mathrm{re}}^{2} \\
&\quad -3\breve{R}_{\mathrm{LOS}}^{3}\breve{R}_{\mathrm{re}}^{3} - \breve{R}_{\mathrm{LOS}}^{3}\breve{R}_{\mathrm{re}}^{3} + 6\breve{D}^{2} + 6\breve{R}_{\mathrm{LOS}}^{2}\breve{D}^{2} + 6\breve{R}_{\mathrm{LOS}}\breve{R}_{\mathrm{re}}\breve{D}^{2} + 6\breve{R}_{\mathrm{LOS}}^{3}\breve{R}_{\mathrm{re}}\breve{D}^{2} - 2\breve{R}_{\mathrm{re}}^{2}\breve{D} - 2\breve{R}_{\mathrm{LOS}}^{2}\breve{R}_{\mathrm{re}}^{2}\breve{D}^{2}),
\end{aligned}$$

$$\begin{aligned}
C_{2,3}^{(7)} &= -\breve{R}_{\mathrm{LOS}}\breve{R}_{\mathrm{re}}^{5}(-3\breve{R}_{\mathrm{LOS}}^{3} - 3\breve{R}_{\mathrm{LOS}}^{5} + 3\breve{R}_{\mathrm{LOS}}^{2}\breve{R}_{\mathrm{re}} + 3\breve{R}_{\mathrm{LOS}}^{4}\breve{R}_{\mathrm{re}} + 3\breve{R}_{\mathrm{LOS}}\breve{R}_{\mathrm{re}}^{2} + 2\breve{R}_{\mathrm{LOS}}^{3}\breve{R}_{\mathrm{re}}^{2} + \breve{R}_{\mathrm{LOS}}^{5}\breve{R}_{\mathrm{re}}^{2} - 3\breve{R}_{\mathrm{re}}^{3} \\
&\quad -2\breve{R}_{\mathrm{LOS}}^{2}\breve{R}_{\mathrm{re}}^{3} - \breve{R}_{\mathrm{LOS}}^{4}\breve{R}_{\mathrm{re}}^{3} - 6\breve{R}_{\mathrm{LOS}}\breve{D}^{2} - 6\breve{R}_{\mathrm{LOS}}^{3}\breve{D}^{2} + 6\breve{R}_{\mathrm{re}}\breve{D}^{2} + 6\breve{R}_{\mathrm{LOS}}^{2}\breve{R}_{\mathrm{re}}\breve{D}^{2} + 2\breve{R}_{\mathrm{LOS}}\breve{R}_{\mathrm{re}}^{2}\breve{D}^{2} + 2\breve{R}_{\mathrm{LOS}}^{3}\breve{R}_{\mathrm{re}}^{2}\breve{D}^{2}),
\end{aligned}$$

$$C_{2,3}^{(8)} = -8\kappa\, \breve{R}_{\mathrm{LOS}}^{5}(1+\breve{R}_{\mathrm{LOS}}^{2})\,(9+3\breve{R}_{\mathrm{re}}^{2}+\breve{R}_{\mathrm{re}}^{4})\breve{D}^{3},$$

$$\begin{aligned}C_{2,3}^{(9)} = {} & 4\kappa \breve{R}_{\mathrm{LOS}}^{4}\breve{D}^{2}\,(27\breve{R}_{\mathrm{LOS}}^{2}+27\breve{R}_{\mathrm{LOS}}^{4}-18\breve{R}_{\mathrm{re}}^{2}-3\breve{R}_{\mathrm{LOS}}^{2}\breve{R}_{\mathrm{re}}^{2}+9\breve{R}_{\mathrm{LOS}}^{4}\breve{R}_{\mathrm{re}}^{2}-12\breve{R}_{\mathrm{re}}^{4}+(\rho_0 c)^2\breve{R}_{\mathrm{re}}^{4}\\ & -5\breve{R}_{\mathrm{LOS}}^{2}\breve{R}_{\mathrm{re}}^{4}+(\rho_0 c)^2\breve{R}_{\mathrm{LOS}}^{2}\breve{R}_{\mathrm{re}}^{4}+3\breve{R}_{\mathrm{LOS}}^{4}\breve{R}_{\mathrm{re}}^{4}-2\breve{R}_{\mathrm{LOS}}^{3}\breve{R}_{\mathrm{re}}^{5}+(\rho_0 c)^2\breve{R}_{\mathrm{re}}^{6}+(\rho_0 c)^2\breve{R}_{\mathrm{LOS}}^{2}\breve{R}_{\mathrm{re}}^{6}\\ & +36\breve{D}^{2}+36\breve{R}_{\mathrm{LOS}}^{2}\breve{D}^{2}+12\breve{R}_{\mathrm{re}}^{2}\breve{D}^{2}+12\breve{R}_{\mathrm{LOS}}^{2}\breve{R}_{\mathrm{re}}^{2}\breve{D}^{2}+4\breve{R}_{\mathrm{re}}^{4}\breve{D}^{2}+4\breve{R}_{\mathrm{LOS}}^{2}\breve{R}_{\mathrm{re}}^{4}\breve{D}^{2}),\end{aligned}$$

$$\begin{aligned}C_{3,3}^{(1)} = {} & (\rho_0 c)^2\breve{R}_{\mathrm{re}}^{10}+\kappa^2(9\breve{R}_{\mathrm{LOS}}^{8}+9\breve{R}_{\mathrm{LOS}}^{10}-18\breve{R}_{\mathrm{LOS}}^{6}\breve{R}_{\mathrm{re}}^{2}-9\breve{R}_{\mathrm{LOS}}^{8}\breve{R}_{\mathrm{re}}^{2}+3\breve{R}_{\mathrm{LOS}}^{10}\breve{R}_{\mathrm{re}}^{2}+9\breve{R}_{\mathrm{LOS}}^{4}\breve{R}_{\mathrm{re}}^{4}\\ & -9\breve{R}_{\mathrm{LOS}}^{6}\breve{R}_{\mathrm{re}}^{4}+(\rho_0 c)^2\breve{R}_{\mathrm{LOS}}^{6}\breve{R}_{\mathrm{re}}^{4}-6\breve{R}_{\mathrm{LOS}}^{8}\breve{R}_{\mathrm{re}}^{4}+(\rho_0 c)^2\breve{R}_{\mathrm{LOS}}^{8}\breve{R}_{\mathrm{re}}^{4}+\breve{R}_{\mathrm{LOS}}^{10}\breve{R}_{\mathrm{re}}^{4}-2\breve{R}_{\mathrm{LOS}}^{9}\breve{R}_{\mathrm{re}}^{5}\\ & +9\breve{R}_{\mathrm{LOS}}^{4}\breve{R}_{\mathrm{re}}^{6}-4(\rho_0 c)^2\breve{R}_{\mathrm{LOS}}^{4}\breve{R}_{\mathrm{re}}^{6}+3\breve{R}_{\mathrm{LOS}}^{6}\breve{R}_{\mathrm{re}}^{6}-(\rho_0 c)^2\breve{R}_{\mathrm{LOS}}^{6}\breve{R}_{\mathrm{re}}^{6}+\breve{R}_{\mathrm{LOS}}^{8}\breve{R}_{\mathrm{re}}^{6}+(\rho_0 c)^2\breve{R}_{\mathrm{LOS}}^{8}\breve{R}_{\mathrm{re}}^{6}\\ & -2(\rho_0 c)^2\breve{R}_{\mathrm{LOS}}^{7}\breve{R}_{\mathrm{re}}^{7}+4(\rho_0 c)^2\breve{R}_{\mathrm{LOS}}^{2}\breve{R}_{\mathrm{re}}^{8}+(\rho_0 c)^2\breve{R}_{\mathrm{LOS}}^{6}\breve{R}_{\mathrm{re}}^{8}+126\breve{R}_{\mathrm{LOS}}^{6}\breve{D}^{2}+126\breve{R}_{\mathrm{LOS}}^{8}\breve{D}^{2}\\ & -108\breve{R}_{\mathrm{LOS}}^{4}\breve{R}_{\mathrm{re}}^{2}\breve{D}^{2}-18\breve{R}_{\mathrm{LOS}}^{6}\breve{R}_{\mathrm{re}}^{2}\breve{D}^{2}+42\breve{R}_{\mathrm{LOS}}^{8}\breve{R}_{\mathrm{re}}^{2}\breve{D}^{2}+16\breve{R}_{\mathrm{LOS}}^{2}\breve{R}_{\mathrm{re}}^{4}\breve{D}^{2}-72\breve{R}_{\mathrm{LOS}}^{4}\breve{R}_{\mathrm{re}}^{4}\breve{D}^{2}\\ & +2(\rho_0 c)^2\breve{R}_{\mathrm{LOS}}^{4}\breve{R}_{\mathrm{re}}^{4}\breve{D}^{2}-22\breve{R}_{\mathrm{LOS}}^{6}\breve{R}_{\mathrm{re}}^{4}\breve{D}^{2}+2(\rho_0 c)^2\breve{R}_{\mathrm{LOS}}^{6}\breve{R}_{\mathrm{re}}^{4}\breve{D}^{2}+14\breve{R}_{\mathrm{LOS}}^{8}\breve{R}_{\mathrm{re}}^{4}\breve{D}^{2}\\ & -16\breve{R}_{\mathrm{LOS}}^{7}\breve{R}_{\mathrm{re}}^{5}\breve{D}^{2}+16\breve{R}_{\mathrm{LOS}}^{2}\breve{R}_{\mathrm{re}}^{6}\breve{D}^{2}+2(\rho_c c)^2\breve{R}_{\mathrm{LOS}}^{4}\breve{R}_{\mathrm{re}}^{6}\breve{D}^{2}+4\breve{R}_{\mathrm{LOS}}^{6}\breve{R}_{\mathrm{re}}^{6}\breve{D}^{2}+2(\rho_0 c)^2\breve{R}_{\mathrm{LOS}}^{6}\breve{R}_{\mathrm{re}}^{6}\breve{D}^{2}\\ & +72\breve{R}_{\mathrm{LOS}}^{4}\breve{D}^{4}+72\breve{R}_{\mathrm{LOS}}^{6}\breve{D}^{4}+24\breve{R}_{\mathrm{LOS}}^{4}\breve{R}_{\mathrm{re}}^{2}\breve{D}^{4}+24\breve{R}_{\mathrm{LOS}}^{6}\breve{R}_{\mathrm{re}}^{2}\breve{D}^{4}+8\breve{R}_{\mathrm{LOS}}^{4}\breve{R}_{\mathrm{re}}^{4}\breve{D}^{4}+8\breve{R}_{\mathrm{LOS}}^{6}\breve{R}_{\mathrm{re}}^{4}\breve{D}^{4}),\end{aligned}$$

$$C_{3,3}^{(2)} = 2\kappa(\rho_0 c)^2\breve{R}_{\mathrm{LOS}}^{2}(\breve{R}_{\mathrm{LOS}}-\breve{R}_{\mathrm{re}})\breve{R}_{\mathrm{re}}^{7}(\breve{R}_{\mathrm{LOS}}+2\breve{R}_{\mathrm{re}}),$$

$$C_{3,3}^{(3)} = 2\kappa\,(\rho_0 c)^2\breve{R}_{\mathrm{LOS}}\breve{R}_{\mathrm{re}}^{7}(-\breve{R}_{\mathrm{LOS}}^{2}+\breve{R}_{\mathrm{LOS}}^{3}\breve{R}_{\mathrm{re}}+2\breve{R}_{\mathrm{re}}^{2}-\breve{R}_{\mathrm{LOS}}^{2}\breve{R}_{\mathrm{re}}^{2}),$$

$$C_{3,3}^{(4)} = -2\kappa\,(\rho_0 c)^2\breve{R}_{\mathrm{LOS}}^{2}\breve{R}_{\mathrm{re}}^{7}(\breve{R}_{\mathrm{LOS}}+\breve{R}_{\mathrm{re}})\,\breve{D},$$

$$C_{3,3}^{(5)} = -2\kappa\,(\rho_0 c)^2\breve{R}_{\mathrm{LOS}}^{2}\breve{R}_{\mathrm{re}}^{7}(-1+\breve{R}_{\mathrm{LOS}}\breve{R}_{\mathrm{re}})\breve{D},$$

$$C_{3,3}^{(6)} = -4\kappa^2\breve{R}_{\mathrm{LOS}}^{5}(1+\breve{R}_{\mathrm{LOS}}^{2})\,(9+3\breve{R}_{\mathrm{re}}^{2}+\breve{R}_{\mathrm{re}}^{4})\breve{D}^{3},$$

$$\begin{aligned}C_{3,3}^{(7)} = {} & 4\kappa^2\breve{R}_{\mathrm{LOS}}^{3}\breve{D}(18\breve{R}_{\mathrm{LOS}}^{4}+18\breve{R}_{\mathrm{LOS}}^{6}-24\breve{R}_{\mathrm{LOS}}^{2}\breve{R}_{\mathrm{re}}^{2}-9\breve{R}_{\mathrm{LOS}}^{4}\breve{R}_{\mathrm{re}}^{2}+6\breve{R}_{\mathrm{LOS}}^{6}\breve{R}_{\mathrm{re}}^{2}+6\breve{R}_{\mathrm{re}}^{4}\\ & -15\breve{R}_{\mathrm{LOS}}^{2}\breve{R}_{\mathrm{re}}^{4}+(\rho_0 c)^2\breve{R}_{\mathrm{LOS}}^{2}\breve{R}_{\mathrm{re}}^{4}-7\breve{R}_{\mathrm{LOS}}^{4}\breve{R}_{\mathrm{re}}^{4}+(\rho_0 c)^2\breve{R}_{\mathrm{LOS}}^{4}\breve{R}_{\mathrm{re}}^{4}+2\breve{R}_{\mathrm{LOS}}^{6}\breve{R}_{\mathrm{re}}^{4}-3\breve{R}_{\mathrm{LOS}}^{5}\breve{R}_{\mathrm{re}}^{5}\\ & +6\breve{R}_{\mathrm{re}}^{2}-2(\rho_0 c)^2\breve{R}_{\mathrm{re}}^{6}+\breve{R}_{\mathrm{LOS}}^{2}\breve{R}_{\mathrm{re}}^{6}+\breve{R}_{\mathrm{LOS}}^{4}\breve{R}_{\mathrm{re}}^{6}+(\rho_0 c)^2\breve{R}_{\mathrm{LOS}}^{4}\breve{R}_{\mathrm{re}}^{6}-(\rho_0 c)^2\breve{R}_{\mathrm{LOS}}^{3}\breve{R}_{\mathrm{re}}^{7}\\ & +63\breve{R}_{\mathrm{LOS}}^{2}\breve{D}^{2}+63\breve{R}_{\mathrm{LOS}}^{4}\breve{D}^{2}-24\breve{R}_{\mathrm{re}}^{2}\breve{D}^{2}+9\breve{R}_{\mathrm{LOS}}^{2}\breve{R}_{\mathrm{re}}^{2}\breve{D}^{2}+21\breve{R}_{\mathrm{LOS}}^{4}\breve{R}_{\mathrm{re}}^{2}\breve{D}^{2}-16\breve{R}_{\mathrm{re}}^{4}\breve{D}^{2}\\ & -\breve{R}_{\mathrm{LOS}}^{2}\breve{R}_{\mathrm{re}}^{4}\breve{D}^{2}+7\breve{R}_{\mathrm{LOS}}^{4}\breve{R}_{\mathrm{re}}^{4}\breve{D}^{2}-4\breve{R}_{\mathrm{LOS}}^{3}\breve{R}_{\mathrm{re}}^{5}\breve{D}^{2}),\end{aligned}$$

$$\begin{aligned}C_{3,3}^{(8)} = {} & -2\kappa^2\breve{R}_{\mathrm{LOS}}^{4}\breve{D}^{2}\,(45\breve{R}_{\mathrm{LOS}}^{2}+45\breve{R}_{\mathrm{LOS}}^{4}-30\breve{R}_{\mathrm{re}}^{2}-3\breve{R}_{\mathrm{LOS}}^{2}\breve{R}_{\mathrm{re}}^{2}+15\breve{R}_{\mathrm{LOS}}^{4}\breve{R}_{\mathrm{re}}^{2}-20\breve{R}_{\mathrm{re}}^{4}+(\rho_0 c)^2\breve{R}_{\mathrm{re}}^{4}\\ & -7\breve{R}_{\mathrm{LOS}}^{2}\breve{R}_{\mathrm{re}}^{4}+(\rho_0 c)^2\breve{R}_{\mathrm{LOS}}^{2}\breve{R}_{\mathrm{re}}^{4}+5\breve{R}_{\mathrm{LOS}}^{4}\breve{R}_{\mathrm{re}}^{4}-4\breve{R}_{\mathrm{LOS}}^{3}\breve{R}_{\mathrm{re}}^{5}+(\rho_0 c)^2\breve{R}_{\mathrm{re}}^{6}+(\rho_0 c)^2\breve{R}_{\mathrm{LOS}}^{2}\breve{R}_{\mathrm{re}}^{6}\\ & +36\breve{D}^{2}+36\breve{R}_{\mathrm{LOS}}^{2}\breve{D}^{2}+12\breve{R}_{\mathrm{re}}^{2}\breve{D}^{2}+12\breve{R}_{\mathrm{LOS}}^{2}\breve{R}_{\mathrm{re}}^{2}\breve{D}^{2}+4\breve{R}_{\mathrm{re}}^{4}\breve{D}^{2}+4\breve{R}_{\mathrm{LOS}}^{2}\breve{R}_{\mathrm{re}}^{4}\breve{D}^{2}).\end{aligned}$$

[1]Uni-axial velocity-sensors have been implemented in hardware for many decades, for both the underwater acoustic medium and for the air acoustic medium (LeBlanc, 1978; Berliner and Lindberg, 1996). Uni-axial velocity-sensors are commercially available as the "Uniaxial P-U Probe" for underwater/sea-surface applications from Acoustech Corporation (U.S.A.).

[2]This acoustic *vector*-sensor concept is practical. It has undergone dozens of underwater/ocean-surface sea trials and many in-room/outdoor air trials. It is commercially available as the "Microflown" for in-room or outdoor air acoustic applications from Microflown Co. (The Netherlands).

[3]The "near field" here may be understood as the spatial region around the emitter, where the wavefield has a significant fraction of its total energy stored in the propagation-medium, i.e., where the wavefield is reactive (like the capacitance or inductance in an electrical system) rather than resistive. More precisely, the near field may be defined as "the emitter-centered spatial region wherein the emitted signal strength decreases monotonically at the rate of 6 dB for each doubling of the distance from the emitter" (p. 264 of Bies and Hansen, 2009). This near field region is spherical, with a radius related to the propagation medium's acoustic characteristic impedance and related to the emitter's spatial size, but *un*related to the sensor's spatial extent. For a point-size emitter, the geometric near field is generally considered as where $R_{\mathrm{LOS}} \ll \lambda$ (Morse and Ingard, 1968) or $R_{\mathrm{LOS}} \ll \lambda/2\pi$ (Hansen, 2005; Bies and Hansen, 2009; Kim, 2010). In contrast, the far field is where the emitted spherical wavefront's specific acoustic impedance approaches the fluid medium's "characteristic acoustic impedance" $\rho_0 c$ (as for a planar wavefront), with no significant imaginary-value part, where ρ_0 denotes the ambient fluid density and c represents the propagation speed. There is an alternative but complementary concept of near field versus far field, defined with respect to the sensor-array's spatial aperture size: When an array of sensors lies sufficiently far from the emitter, the incident wavefront would appear effectively planar across the array's geometric aperture. However, in this present investigation, the sensors' spatial aperture is not at issue, as the acoustic vector-sensor's component-sensors are collocated. Hence, this other concept of near field is irrelevant here.

[4]This paper assumes the reflecting plane to coincide with a Cartesian plane (namely, a plane parallel to the x-y plane in Fig. 1), for mathematical simplicity. If not parallel, simply define a new set of Cartesian coordinates (x', y', z')), which may be rotated back to the present (x, y, z) coordinates via an appropriate set of Euler angles, such that the reflecting boundary will be parallel to the $x' - y'$ plane.

[5]This Eq. (19) represents a special case of the subsequent Eq. (23).

[6]However, the definition of ψ in Wu *et al.* (2010) differs from the present paper's.

[7]Of the *far*-field *no*-boundary measurement model of Nehorai and Paldi (1994), its corresponding Cramér-Rao lower bound for direction finding has been derived analytically in Nehorai and Paldi (1994), Hawkes and Nehorai (1999), Tichavsky *et al.* (2001), Tam and Wong (2009), Li *et al.* (2011), Zhong *et al.* (2012), Song and Wong (2012), and Tam *et al.* (2014). For the not-necessarily-far-field *no*-boundary measurement model of Wu *et al.* (2010), its corresponding Cramér-Rao lower bound for azimuth/elevation/distance 3D source localization is derived analytically in Wu *et al.* (2010) and Yuan (2012). For the *far*-field *near*-boundary measurement model of Hawkes and Nehorai (2000), the corresponding Cramér-Rao lower bound for direction finding has been derived analytically in Hawkes and Nehorai (2000, 2003) and Ahmadi-Shokouh and Keshavarz (2007).

[8]These following results could also be obtained directly by setting $\theta = [\phi, \psi, \sigma^2]^T$, for substitution into Eq. (28).

[9]Besides the maximum likelihood approach, many other signal-processing algorithms have been developed for the acoustic vector-sensor for adaptive beamforming, source localization, direction finding, and tracking. Please refer to the surveys in Tam and Wong (2009), Wu and Wong (2012), Wu *et al.* (2012), and Awad and Wong (2012).

[10]So long as $\epsilon_1 - \epsilon_2$ is unequal to any integer multiple of π (thereby avoiding perfect in-phase or anti-phase summation of the two waves), the graph would look essentially similar to Fig. 17.

[11]So long as $\epsilon_1 - \epsilon_2$ is unequal to any integer multiple of π (thereby avoiding perfect in-phase or anti-phase summation of the two waves), the graph would look essentially similar to Fig. 18.

Ahmadi-Shokouh, J., and Keshavarz, H. (**2007**). "A vector-hydrophone's minimal composition for finite estimation-variance in direction-finding near/without a reflecting boundary," IEEE Trans. Signal Process. **55**, 2785–2794.

Attenborough, K. (**2002**). "Sound propagation close to the ground," Annu. Rev. Fluid. Mech. **34**, 51–82.

Awad, M. K., and Wong, K. T. (**2012**). "Recursive least-squares source-tracking using one acoustic vector-sensor," IEEE Trans. Aero. Elec. Sys. **48**, 3073–3083.

Berliner, M. J., and Lindberg, J. F., eds. (**1996**). *Acoustical Particle Velocity Sensors: Design, Performance and Applications* (AIP Press, Woodbury, New York), pp. 1–434.

Bies, D. A., and Hansen, C. H. (**2009**). *Engineering Noise Control* (Taylor & Francis, London, United Kingdom), pp. 1–768.

Buckingham, M. J., and Tolstoy, A. (**1990**). "An analytical solution for benchmark problem 1: The 'ideal' wedge,"' J. Acoust. Soc. Am. **87**, 1511–1513.

Embleton, T. F. W., Piercy, J. E., and Olson, N. (**1976**). "Outdoor sound propagation over ground of finite impedance," J. Acoust. Soc. Am. **59**, 267–277.

Felisberto, P., Schneiderwind, J., Santos, P., Rodriguez, O., and Jesus, S. (**2012**). "Comparing the resolution of Bartlett and MVDR estimators for bottom parameter estimation using pressure and vector sensor short array data," in *IEEE/MTS Oceans*.

Gumerov, N. A., and Duraiswami, R. (**2001**). "Modeling the effect of a nearby boundary on the HRTF," in *IEEE International Conference of Acoustics, Speech, and Signal Processing*, pp. 3337–3340.

Hansen, C. (**2005**). *Noise Control: From Concept to Application* (Taylor & Francis, London, United Kingdom), pp. 1–432.

Hawkes, M., and Nehorai, A. (**1999**). "Effects of sensor placement on acoustic vector-sensor array performance," IEEE J. Ocean. Eng. **24**, 33–40.

Hawkes, M., and Nehorai, A. (**2000**). "Acoustic vector-sensor processing in the presence of a reflecting boundary," IEEE Trans. Signal Process. **48**, 2981–2993.

Hawkes, M., and Nehorai, A. (**2003**). "Wideband source localization using a distributed acoustic vector-sensor array," IEEE Trans. Signal Process. **51**, 1479–1491.

Kim, Y. H. (**2010**). *Sound Propagation: An Impedance Based Approach* (John Wiley & Sons, Singapore, Japan), pp. 1–416.

Ko, S. H., ed. (**1996**). *Acoustical Particle Velocity Sensors: Design, Performance and Applications* (AIP Press, Woodbury, New York), pp. 374–389.

LeBlanc, C. L. (**1978**). "Handbook of hydrophone element design technology," J. Acoust. Soc. Am. **64**, S167–S167.

Leighton, T. G. (**2012**). "How can humans, in air, hear sound generated underwater (and can goldfish hear their owners talking)?," J. Acoust. Soc. Am. **131**, 2539–2542.

Levin, D., Habets, E. A. P., and Gannot, S. (**2010**). "On the angular error of intensity vector based direction of arrival estimation in reverberant sound fields," J. Acoust. Soc. Am. **128**(7), 1800–1811.

Li, K. M., and Lu, K. K. (**2004**). "Propagation of sound in long enclosures," J. Acoust. Soc. Am. **116**, 2759–2770.

Li, T., Tabrikian, J., and Nehorai, A. (**2011**). "A Barankin-type bound on direction estimation using acoustic sensor arrays," IEEE Trans. Signal Process. **59**, 431–436.

Luo, W. Y., Yang, C. M., Qin, J. X., and Zhang, R. H. (**2012**). "Sound propagation in a wedge with a rigid bottom," Chin. Phys. Lett. **29**, 1–4.

Morse, P. M., and Ingard, K. U. (**1968**). *Theoretical Acoustics* (Princeton University Press, NJ), pp. 1–913.

Nagananda, K. G., and Anand, G. V. (**2010**). "Subspace intersection method of high resolution bearing estimation in shallow ocean using acoustic vector sensors," Signal Process. **90**, 105–118.

Nehorai, A., and Hawkes, M. (**2000**). "Performance bounds for estimating vector systems," IEEE Trans. Signal Process. **48**, 1737–1749.

Nehorai, A., and Paldi, E. (**1994**). "Acoustic vector-sensor array processing," IEEE Trans. Signal Process. **42**, 2481–2491.

Pierce, A. D. (**1989**). *Acoustics—An Introduction to its Physical Principles and Applications* (McGraw-Hill, New York), pp. 1–678.

Remillieux, M. C. (**2012**). "External pressure loading, vibration, and acoustic responses at low frequencies of building components exposed to impulsive sound," Appl. Acoust. **73**, 1059–1075.

Song, Y., and Wong, K. T. (**2012**). "Lower bound of direction-of-arrival estimation for acoustic vector sensor with sensor breakdown," IEEE Trans. Aero. Elec. Sys. **48**, 3703–3708.

Stinson, M. R. (**1995**). "A note on the use of an approximate formula to predict sound fields above an impedance plane due to a point source," J. Acoust. Soc. Am. **98**, 1810–1812.

Tam, P. K., and Wong, K. T. (**2009**). "Cramer-Rao bounds for direction finding by an acoustic vector sensor under nonideal gain-phase responses, noncollocation, or nonorthogonal orientation," IEEE Sens. J. **9**, 969–982.

Tam, P. K., Wong, K. T., and Song, Y. (**2014**). "An hybrid Cramér-Rao bound in closed form for direction-of-arrival estimation by an 'acoustic

vector sensor' with gain-phase uncertainties," IEEE Trans. Signal Process. **62**, 2504–2516.
Tichavsky, P., Wong, K. T., and Zoltowski, M. D. (**2001**). "Near-field/far-field azimuth and elevation angle estimation using a single vector hydrophone," IEEE Trans. Signal Process. **49**, 2498–2510.
Van-Trees, H. L. (**2002**). *Detection, Estimation, and Modulation Theory, Part IV: Optimum Array Processing* (Wiley, New York), Chap. 8.4, pp. 938–980.
Wu, Y. I., and Wong, K. T. (**2012**). "Acoustic near-field source localization by two passive anchor nodes," IEEE Trans. Aero. Elec. Sys. **48**, 159–169.
Wu, Y. I., Wong, K. T., and Lau, S. K. (**2010**). "The acoustic vector-sensor's near-field array-manifold," IEEE Trans. Signal Process. **58**, 3946–3951.
Wu, Y. I., Wong, K. T., Lau, S.-K., Yuan, X., and Tang, S. K. (**2012**). "A directionally tunable but frequency-invariant beamformer on an acoustic velocity-sensor triad to enhance speech perception," J. Acoust. Soc. Am. **131**, 3891–3902.
Yuan, X. (**2012**). "Cramér-Rao bounds of direction-of-arrival and distance estimation of a near-field incident source for an acoustic vector sensor: Gaussian source and polynomial-phase source," IET Radar, Sonar, Nav. **6**, 638–648.
Zhong, X., Premkumar, A. B., and Madhukumar, A. S. (**2012**). "Particle filtering and posterior Cramer-Rao bound for 2-d direction of arrival tracking using an acoustic vector sensor," IEEE Sens. J. **12**, 363–377.